OAK RIDGE NATIONAL LABORATORY LIBRARIES
3 4456 0555902 6
OAK RIDGE NATIONAL LABORATORY LIBRARIES

CENTRAL RESEARCH LIBRARY

ORNL-TM-4587

Cy 71

AQUEOUS FUEL REPROCESSING QUARTERLY REPORT FOR PERIOD ENDING MARCH 31, 1974

W. E. Unger
V. C. A. Vaughen
A. R. Irvine
C. D. Watson

[redacted]

OAK RIDGE NATIONAL LABORATORY
CENTRAL RESEARCH LIBRARY
DOCUMENT COLLECTION
LIBRARY LOAN COPY
DO NOT TRANSFER TO ANOTHER PERSON
If you wish someone else to see this document, send in name with document and the library will arrange a loan.
UCN-7969
(3 3-67)

OAK RIDGE NATIONAL LABORATORY
OPERATED BY UNION CARBIDE CORPORATION • FOR THE U.S. ATOMIC ENERGY COMMISSION

Printed in the United States of America. Available from
the U.S. Atomic Energy Commission, Technical Information Center
P.O. Box 62, Oak Ridge, Tennessee 37830
Price: Printed Copy $5.45 ; Microfiche $1.45

This report was prepared as an account of work sponsored by the United States Government. Neither the United States nor the United States Atomic Energy Commission, nor any of their employees, nor any of their contractors, subcontractors, or their employees, makes any warranty, express or implied, or assumes any legal liability or responsibility for the accuracy, completeness or usefulness of any information, apparatus, product or process disclosed, or represents that its use would not infringe privately owned rights.

ORNL-TM-4587
UC-79c - Fuel Recycle

Contract No. W-7405-eng-26

CHEMICAL TECHNOLOGY DIVISION

AQUEOUS FUEL REPROCESSING QUARTERLY REPORT FOR PERIOD ENDING MARCH 31, 1974

W. E. Unger, V. C. A. Vaughen,
A. R. Irvine, C. D. Watson

SEPTEMBER 1974

NOTICE This document contains information of a preliminary nature and was prepared primarily for internal use at the Oak Ridge National Laboratory. It is subject to revision or correction and therefore does not represent a final report.

OAK RIDGE NATIONAL LABORATORY
Oak Ridge, Tennessee 37830
operated by
UNION CARBIDE CORPORATION
for the
U.S. ATOMIC ENERGY COMMISSION

3 4456 0555902 6

OAK RIDGE NATIONAL LABORATORY LIBRARIES

CONTENTS

		Page
Highlights		1
1.	Shipping (Task 1)	3
2.	Receiving and Storage (Task 2)	3
3.	Head-End Processing of LMFBR Fuels (Task 3)	4
4.	Volatile Fission Product Removal (Task 4)	27
5.	Dissolution (Task 5)	34
6.	Feed Preparation (Task 6)	41
7.	Solvent Extraction (Task 7)	41
8.	Plutonium Purification (Task 8)	41
9.	Waste Treatment and Storage (Task 9)	41
10.	Off-Gas Treatment (Task 10)	42
11.	Engineering Studies (Task 11)	58

AQUEOUS FUEL REPROCESSING QUARTERLY REPORT FOR PERIOD ENDING MARCH 31, 1974

HIGHLIGHTS

Disassembly. - Plasma-arc cropping of the gas plenum sections of fuel assemblies has resulted in highly acceptable cut faces with as little as 5% of the tube faces closed. The method does not appear to be feasible for disassembly or rod pulling. A nonconsumable rotary electrode cutting technique is being investigated as an alternative to the plasma-arc method. The new method appears to be applicable to cropping, slitting, circumferential cutting, and waste consolidation. (Sect. 3.2)

Shearing. - The characterization of the sheared product resulting from various combinations of shear blades, compactor shapes, and gas wrapper ductility was completed with prototype fuel containing porcelain as a stand-in for urania-plutonia. The development and initial testing of a sequential forming gag-compactor was completed, and modifications to the gull-wing compactor are being made. (Sect. 3.3)

The first series of voloxidizer optimization studies with HEDL PNL X-7 fuel yielded the interesting information that the amount of residual tritium after voloxidation appears to be highly dependent on the sample position in the fuel rod. (Sect. 4)

The temperature of voloxidation (550°C or 650°C) increased the amount of insoluble residue after 2 hr leaching in 8 *M* HNO_3 by 0.01 to 0.03% of the total fuel for the higher power levels (≥ 10 kW/ft). (Sect. 5)

Insoluble residue particle sizes were found to be between about 0.5 μ and about 40 μ. Settling tests indicated that about 50% of the residue was in the range 8 to 20 μ and about 50% of the residue was in the range 20 to 40 μ. (Sect. 5).

Deactivating the fluoride with boron, as a potential soluble poison or as a corrosion inhibitor, did not destroy the effectiveness of the fluoride in dissolving the nitric-acid-insoluble residues. (Sect. 5)

Nimonic PE-16 and embrittled type 446 stainless steels were severely attacked by 8 *M* HNO_3–0.05 *M* HF. (Sect. 5)

Static-bed hull rinsing tests in engineering-scale equipment were inadequate to recover simulated HNO_3-insoluble fines. (Sect. 5)

Rotary dissolver hull rinsing tests in a 12-in.-diam dissolver removed > 99.5% of simulated HNO_3 insoluble fines. (Sect. 5)

Design on a 48-in.-diam rotary dissolver for materials transport tests, seal evaluation, and off-gas control studies has been started. (Sect. 5)

Continued tests of the Iodox system in a seven-plate bubble-cap tower indicate stage decontamination factors in the range of 3 to 35 with no decrease in efficiency with high CO_2 concentrations in the feed gas. (Sect. 10.1)

Shakedown runs of a bench-scale system for concentrating nitric acid to 22 *M* for use in the Iodox system were started. The acid concentration flowsheet is based on an extractive distillation process using magnesium nitrate. (Sect. 10.2)

Studies of the chemistry of the Iodox system were continued and equilibrium reactions and coefficients for the oxidization of I^0 to I^+ in the concentrated nitric acid—nitrous oxide system are reported. (Sect. 10.4)

Studies of a plant system for removing volatile fission products from off-gas indicate that nitrogen oxide removal and final iodine removal processes can benefit from operating with compressed and dried gases that are required by the noble gas removal equipment. (Sect. 11)

1. SHIPPING (TASK 1)

(A. R. Irvine, L. B. Shappert, and B. B. Klima)

The objective of Task 1 is to ensure that a safe and economic method of transporting LMFBR spent fuel will be available when needed for transport of fuel from demonstration and early commercial LMFBRs. We have established in principle that a high degree of resistance to fire and impact can be obtained in a cask made of steel and fitted with special access closures and thermal shield. The major issue at this time concerns the degree of resistance to hazards that an LMFBR fuel cask must possess.

There is no progress to report.

2. RECEIVING AND STORAGE (TASK 2)

This task is concerned with the means for rapid, effective, economical, and safe operation of receiving and storage facilities for LMFBR fuels.

No work was performed on this task.

3. HEAD-END PROCESSING OF LMFBR FUELS (TASK 3)

(C. D. Watson)

The objectives of this task are to develop economic head-end processing steps, in preparation for Purex recovery methods, for long- and short-decayed fuels.

3.2 Disassembly (Task 3.2)

(C. D. Watson, R. B. Heimdahl, W. F. Schaffer, Jr., J. C. Rose, C. H. Wodtke,* and W. A. Plunkett*

The removal or cropping of the gas plenum section and its companion end adapter from LMFBR subassemblies is being investigated as a means of minimizing the amount of unfueled stainless steel and tramp sodium reporting to the downstream reprocessing steps. The complete disassembly of a subassembly involving the removal or withdrawal of all of the 217 fuel rods contained in the wrapper is also being investigated as a backup method. This subprogram involves the circumferential cutting of the adapter on the end of the subassembly opposite the gas plenum section where a clearance of $\sim$ 30 mils exists between the wrapper and end fitting. Presently, longitudinal slitting of the wrapper is not being investigated because of the projected use of fuel rod grid spacers spot welded to the wrapper.

During this report period some cropping and gouging cutting tests were conducted in the field with a jury rigged plasma-arc torch and gouging equipment; the temperature attained by the empty fuel tubes during cropping was estimated with crude sensors; a new plasma-arc cutting unit was designed and fabricated and a new cutting process option was investigated and an evaluation program of the method begun via commercial consultation and field tests. Another, but somewhat dubious cutting option, is also being investigated but no tests have been made as yet.

In the plasma-arc removal of the gas plenum section from prototype LMFBR fuel, it is desirable to leave the severed tube openings as free as possible of molten metal. If the tubes become completely closed, leach acid in the dissolver would have only one passage for entry and contact with the spent fuel. We have now essentially completed our field plasma-arc cutting tests and our best cuts (using an initial cut and a trim cut) leave from about 8 to 14 of the 217 tube faces closed with molten metal. We have not been able to improve this situation despite many trial cuttings during which the various cutting parameters were changed appropriately.

---

*P & E Division

The equipment and parameters producing cuts with only about (4-7%) of the tube faces closed are:

torch model:	PT-7, stationary mode
torch tip:	4X12 (4/32-in.-diam orifice by 12/32-in. long)
torch angle:	12° to 15° from the vertical
starting gas:	50% argon — 50% nitrogen
cutting gas:	35% hydrogen — 65% argon, 210 scfh
rotational speed of subassembly:	2.5 rpm
startup time:	2 sec
total cutting time:	32 to 45 sec.

Once the plenum is severed at these conditions, the torch (set at the same angle) is moved 5/8 in. away from the initial cut and a trim cut is made. The trim cut is essential in minimizing the number of tubes with closed faces.

Several circumferential plasma-arc cuts were made on a crude prototype subassembly simulating the end of a subassembly opposite the gas plenum section. At this location, severing of the shroud and inner sleeve unit (with an annular spacing of 30 mils) would allow the withdrawal of all of the 217 fuel rods as a single bundle. Although the prototype was easily severed by the torch, the 30-mil annulus filled with molten metal and welded itself together. Removal of the inert end adapter from a subassembly such that the 217 captive fuel rods could be withdrawn as a single bundle was also attempted by "gouging." The section being gouged by the welding torch partially rewelded itself together from the resulting melt and the method does not look sufficiently promising to continue its development.

A 217-pin prototype LMFBR subassembly bundle, simulating the transition of a gas plenum section with a fueled section, was cut with the plasma-arc torch in an attempt to determine the axial temperature profile near the face of the cut. Temperature sensitive paint and "Tempilstik" temperature indicating crayons were applied to 34 of the 217 pins, and these marked pins were distributed in a "cross" pattern from flat-to-flat and across the diagonal of the hexagonal subassembly. The cut was made 1 in. from the end of the stand-in porcelain fuel with the torch inclined 15° from the vertical. The subassembly was rotated at 2-1/2 rpm under a 4X12* cutting tip. Analysis of the temperature profile was then made (see Fig. 3-1) after disassembling the hexagonal subassembly.

It was found that two major temperature zones could be distinguished with the rather crude sensors: (a) the outermost cooler rods, and (b) the hotter inner rods, which, in several cases, were generally closed

*4/32-in.-diam orifice by 12/32 in. long.

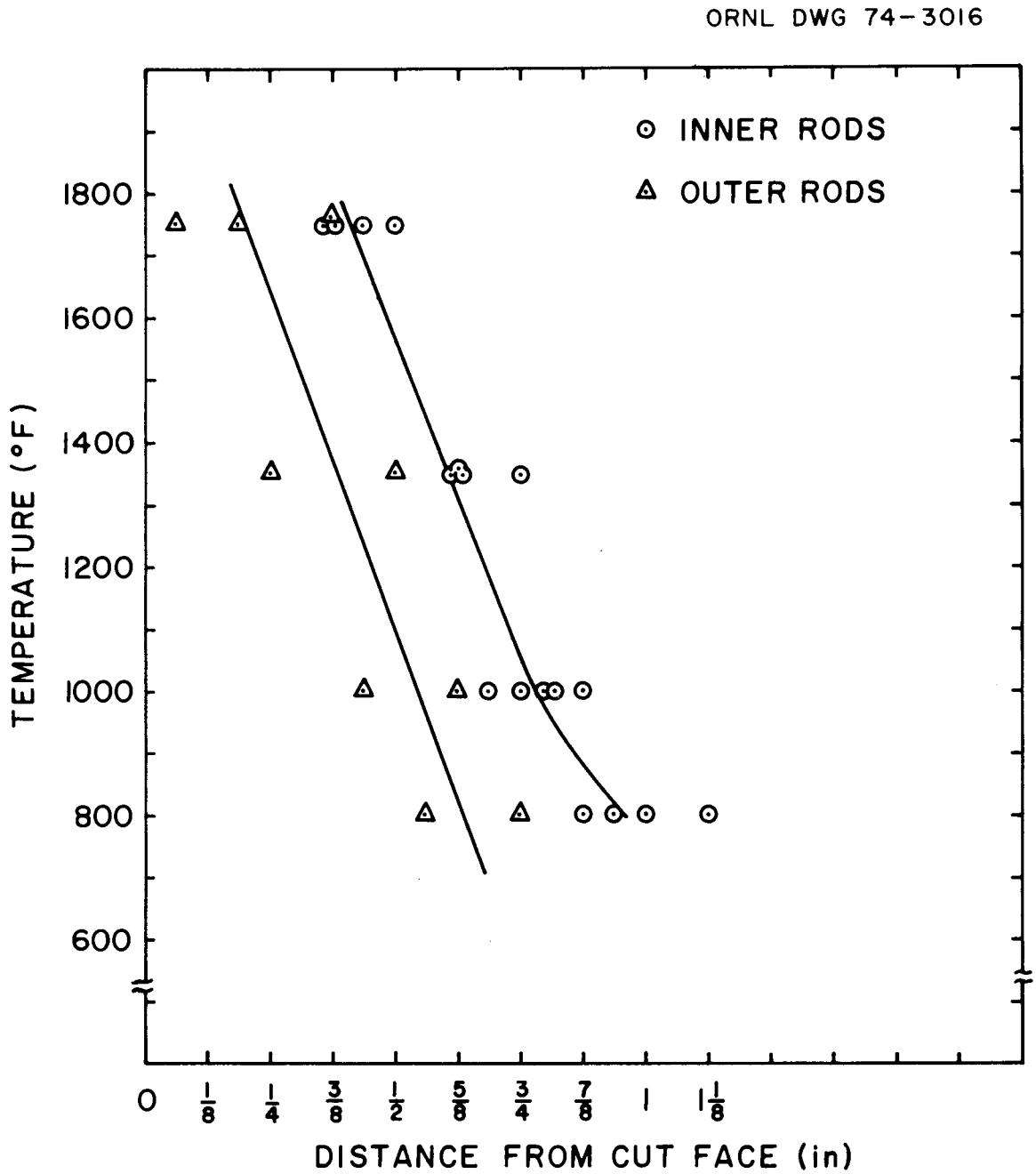

Fig. 3-1. Axial Temperature Profile of a Prototype Gas Plenum Section Severed by a Plasma-Arc Torch.

with molten metal. The thermal gradient for the outer rods was ∿ 1800°F/in. over a temperature range of 1800°F to 1000°F. The average temperature at a point 3/16 in. from the cut was 1800°F and < 800°F at the face of the stand-in fuel. The hotter, innermost rods show an average temperature of 1800°F at a point 3/8 in. from the cut with a gradient of ∿ 2300°F/in. and 800°F at the face of the stand-in fuel.

Plasma-arc torch cutting equipment has been designed and fabricated and is presently being installed in the Experimental Engineering Section to obtain definitive design data for scaling up to the large scale engineering experiment level. The equipment is contained in the following engineering drawings: M-11244-CD-060-D and M-11244-CD-061 through -067E.

The cropping and dismantling of LMFBR fuel using a non-consumable rotary electrode system developed by Schlienger, Inc., San Rafael, California, superficially appears to be more versatile and superior to the plasma-arc torch system now being developed for this purpose. The patents of this cutting method expired some 20 years ago. However, Schlienger, Inc. innovative control and cooling systems in conjunction with the expired patents extend the use of an old idea into new fields. Presently, they are the sole source of this type of cutting technology. Schlienger does not manufacture standard equipment components, rather customizing the units to fit the particular need and requirements of the user. The Chemical Technology Division has engaged Schlienger, Inc. in a consultation and testing capacity to evaluate their method for our proposed use. In this respect, they will perform the following cutting and melting tests.

1. Traverse cutting (cropping) through the gas plenum section and at the opposite end adapter section where the stainless steel insert mates with the gas wrapper at a clearance of 30 mils.
2. Longitudinal cutting of the hexagonal gas wrapper at opposite corners and flats plus slitting of the cladding of simulated fuel rods.
3. Trial melting tests of stainless steel prototype hulls, wires, simulated wrappers, and end adapters and casting of the melt into ingots.

It is expected that Schlienger, Inc. in conjunction with ORNL engineers will perform the cuttings tests outlined above, evaluate the cutting method, and determine the feasibility of continuing the development of the method for head-end processing of LMFBR fuel. Also, ORNL expects to determine the feasibility of using the rotating electrode for melting and disposing of the waste stainless steel produced during the reprocessing of spent fuel.

A formal report will be prepared of the overall test program in which the cutting and melting data are analyzed, recommendations for future action made, and appropriate cost estimates given. The report

is to be supported and substantiated by specimens cut and melted from the materials supplied by ORNL.

If the program is successful, it is likely that ORNL will enter into a contract with Schlienger, Inc. to produce the equipment components for the LMFBR Cold Large-Scale Engineering Test Program.

Recently, a Jetcord explosive method of severing the gas plenum or fueled sections in a microsecond using a shaped charge (Munroe effect) was reviewed. The method appears sufficiently promising to possibly warrant a demonstration test on prototype subassemblies. We will contact the Explosive Technology Company to explore their willingness to make such a test and continue to study it on a minor subprogram level as a process option.

3.3 Shearing (Task 3.3)

(C. D. Watson, R. B. Heimdahl, W. F. Schaffer, Jr., and J. C. Rose)

Studies of converting cropped prototype LMFBR subassemblies into a sheared product easily handleable downstream in the voloxidation/internal sodium deactivation and dissolution steps were continued as follows:

a. interior alterations to the ORNL 250-ton bundle shear,

b. design and fabrication of new shear blades,

c. design and modeling of a new gag-compactor system, and

d. subassembly field and in-shear compaction tests with a concomitant shearing and sheared product characterization analysis.

A new open-throated ram which carries the moving shear blade, across the face of the fixed blade, was designed, fabricated, and installed in the ORNL 250-ton bundle shear. The old ram, a stainless steel casting with a severely restricted throat (based on outmoded criticality considerations), was replaced with a new unit fabricated from hot rolled steel plate. The new unit allows the sheared product to fall free with little or no holdup and it can be drilled and tapped easily to accommodate the new shear blade designs. The cost of the unit was approximately $15,000.

One of the principal problems in shearing LMFBR fuel is that of breaking the 1/8-in.-thick wrapper or shroud into pieces sufficiently short such that they can be transported downstream without clogging of the shear discharge and transport ducts. In an attempt to solve this problem a segmented moving shear blade was designed and fabricated, as shown in Fig. 3-2. It is now being readied for evaluation testing. The three leading blade fingers penetrate completely through the subassembly and the straight faced trailing blade segment then shears off the two remaining portions (shown crosshatched) of the subassembly. The entire

ORNL DWG 74-3008

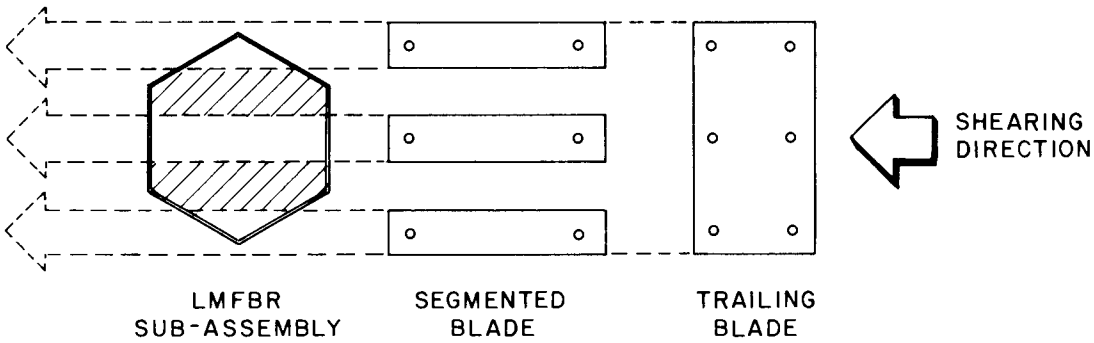

Fig. 3-2. Experimental Segmented Shear Blade.

sequence takes place in a single forward stroke of the shear. Other blade concepts are presently being made for a continuation of this study.

The design of the LWR fuel holding device, called a "gag", that restrains a fuel subassembly while it is being sheared is not applicable to the heavily shrouded LMFBR fuel. A new gag-compactor has been designed that can crush an LMFBR subassembly sufficiently to prevent the fuel rods and wire spacers from being pulled forward into the shear while they are being sheared. A wood-plastic model is presently being made to validate some of the main design features prior to fabrication of an in-shear unit in the machine shop.

Various compactor shapes are also being studied to determine the contour that produce the most desirable effects on the sheared product. Two basic compactor shapes were developed and modified; the gull-wing shape,[1] and the M-shape. These were investigated as to their ability to reduce the cross-sectional area of the prototype fuel assemblies, as well as minimizing the breakup of the 1/8-in.-thick stainless steel wrapper. The breakup of the wrapper decreases its ability to contain the fuel rods during subsequent feeding of the subassembly to the shear.

A concept for a compactor which acts to progressively compact the subassembly over an 8-in. length was proposed. A series of four simple compactor shapes with increasing degrees of compaction were fabricated, for the initial tests of this concept. These simple shapes were then tested on a hydraulic press, by sequentially compacting a 4-in.-long porcelain-filled prototype fuel assembly. The four shapes used for the sequential forming test are shown in Fig. 3-3, along with an overlay of tracings of the fuel assembly after being compacted by each of the compactor shapes. The results of these tests were sufficiently encouraging to have a single compactor machined to accomplish the sequential forming operation. Each of the four shapes tested represent cross-sectional profiles at various positions along the length of the single compactor. This required that a transition be made from a half-hexagon profile at one end, to a full M-shape at the other end of an 8-in.-long piece. The machining problems were sufficient to require that this work be done on a computer-tape controlled, three-axis milling machine. After completing the fabrication of this sequential forming gag, its performance was tested by progressively compacting a 15-in.-long embrittled prototype fuel assembly. The first compaction was made with 1 in. of the assembly extending beneath the compactor, and subsequent pressings were made after feeding the assembly in 1-in. increments. A small crack developed in the wrapper after 6 in. of the assembly had been compacted, but the crack did not propagate appreciably during subsequent compactions. In-shear compaction tests are planned next with this compactor.

The gull-wing compactor shape was modified to increase the bend radius that the fuel assembly is subjected to during compaction. The results of compaction tests performed with the gull-wing compactor in a machine shop hydraulic press are shown in Fig. 3-4. These tests were

ORNL DWG 74-3025

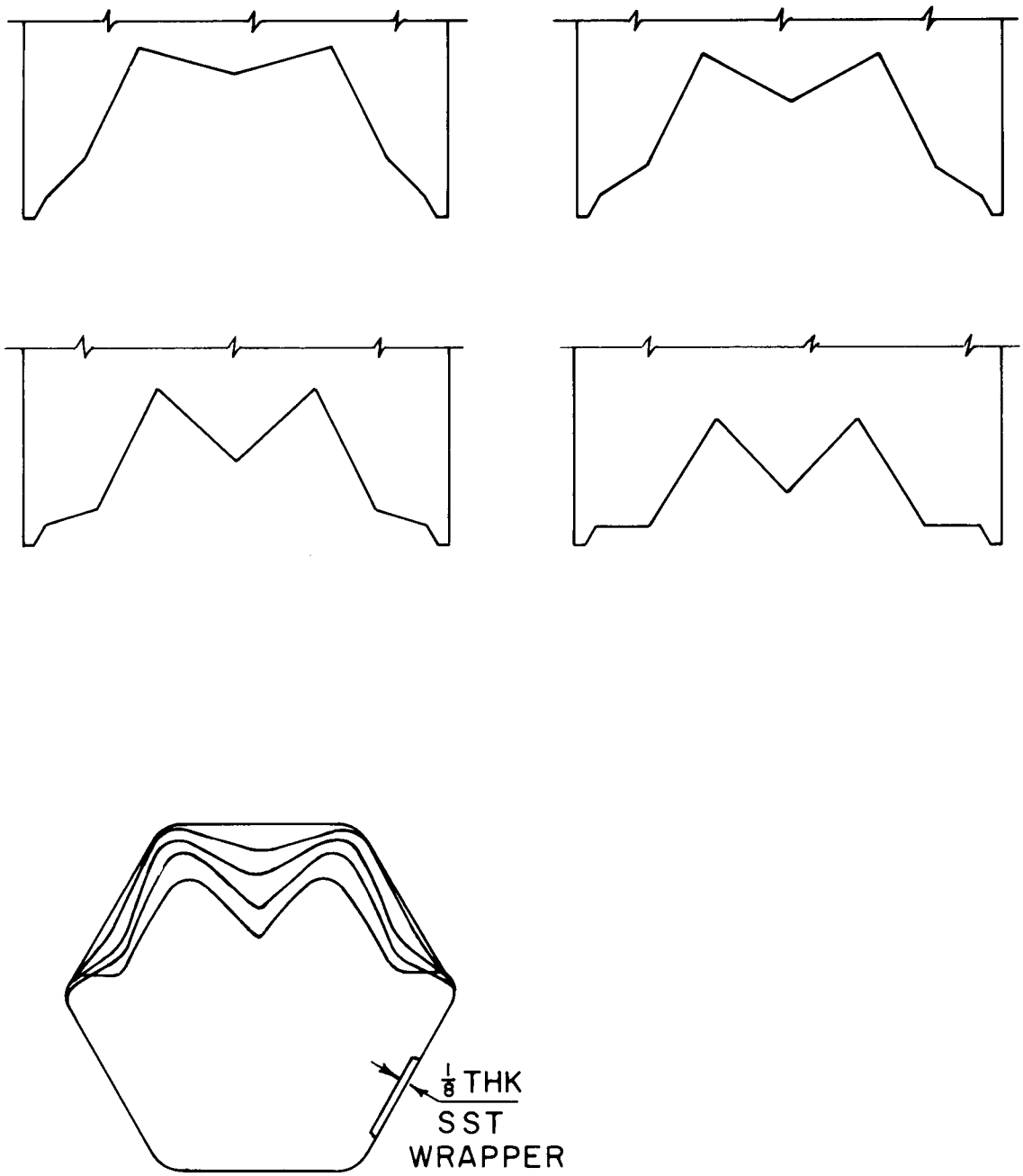

Fig. 3-3. Sequential Forming Compactor Test Results.

ORNL DWG 74-3024

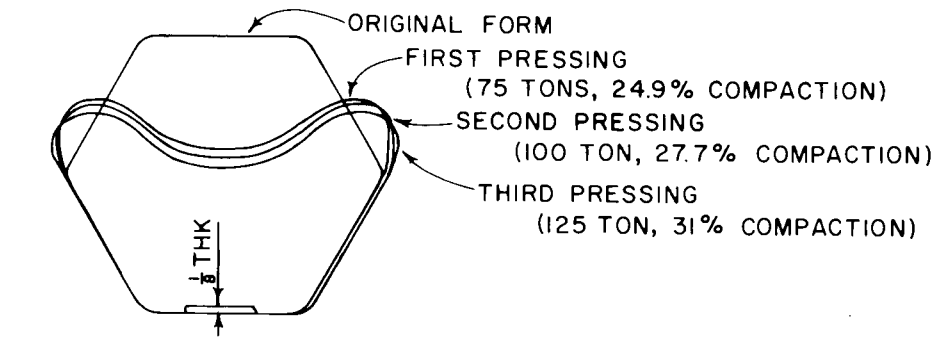

GULL-WING COMPACTION TEST

Fig. 3-4. Compaction Test Results with Gull-Wing Compactor.

performed by sequentially increasing the applied force to the compactor, and tracing the resulting shapes of the compacted fuel assembly. The final degree of compaction attained with 125 tons applied force was 31%. This degree of compaction has been proven to constrain the bundle sufficiently during shearing to prevent the fuel pins from being pulled longitudinally from the fuel assembly during shearing.

The design of a sequential forming compactor having a transition from a half-hexagon profile to the gull-wing profile was completed. This compactor is also being machined on a computer-tape controlled three-axis milling machine at the Y-12 Plant, and should be ready for testing shortly. Two additional compactor designs based on the gull-wing profile have been designed and are being fabricated. These compactors are shown in Fig. 3-5. The Type II design is intended to prevent flaring out of the fuel assembly as it is being compacted. This design should better accommodate the withdrawal of a compacted subassembly from the shear. The Type III design is expected to minimize the bending stresses in the fuel subassembly wrapper by limiting all bending radii to 1.125 in. Hopefully, by limiting the bending radii to this value, the embrittled stainless steel wrappers will maintain their constraint on the fuel pins by not fracturing.

Product Characterization — The characterization of the product resulting from the shearing of whole fuel subassemblies is essential to the design of most process equipment downstream of the shear. The 217-pin fuel subassemblies are contained in a hexagonal array with a 1/8-in.-thick stainless steel wrapper. The shearing operation consists of feeding the subassemblies to the shear, compacting the subassembly, and shearing into 1-in. lengths. Compaction of the subassembly is necessary to prevent the individual fuel pins from being pulled axially out of the subassembly by the large forces necessary to shear. Ideally, the 1/8-in.-thick stainless steel wrapper would be fragmented into a large number of small, easily handled pieces by the combined action of the gag-compactor mechanism and the shear blade. This condition would considerably reduce the requirements of all solids handling devices.

A test program was set up to obtain comparisons between the product generated under various conditions, including gag-compactor shape, shear blade design, and ductility of the stainless steel. Under prolonged conditions of high neutron flux, the stainless steel fuel pins and wrapper become embrittled. The effect of this embrittlement has recently been simulated by an appropriate heat treatment of 446 stainless steel. Several prototype fuel subassemblies have been fabricated of porcelain-filled 446 stainless steel, with some of these left in their normal, ductile state, while several specimens were embrittled. These trial subassemblies were cut into ∿ 4-in.-long segments and sheared into ∿ 1-in.-long pieces. The ability of the gag-compactor mechanism to restrain the ∿ 1-in.-long terminal piece was thus also observed.

Two types of gag-compactor shapes were tested. These are designated as the gull-wing-shape and the M-shape, by virtue of the appearance of

ORNL DWG 74-3026 R1

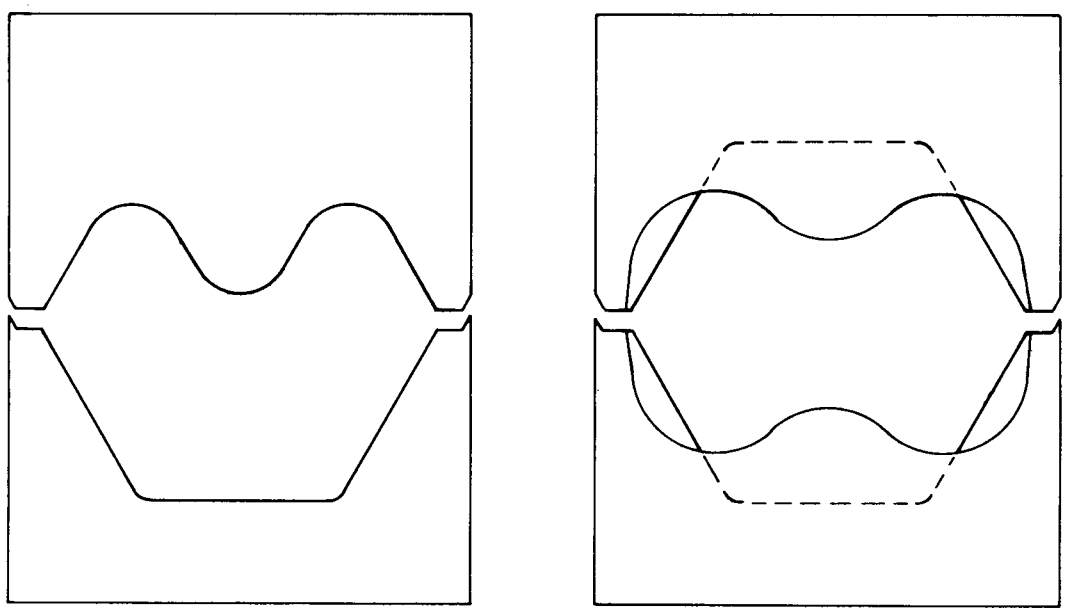

GULL-WING COMPACTOR TYPE II

TOP AND BOTTOM GULL-WING COMPACTOR TYPE III

Fig. 3-5. Type II and Type III Gull-Wing Compactors.

their profiles. Three different shear blades were also used. These blades were all essentially stepped blades, with one of these having an elongated central section to pierce completely through the sub-assembly before the remaining steps begin shearing. One of these blades was a modified version of a stepped blade, in which the blade was provided with a 45° chisel-point, in contrast with the square shearing face of the others.

The shearing tests were performed with the various combinations of gag-compactor, shear-blade design, and ductility indicated in Table 3-1.

Table 3-1. Shearing Combinations

Ductility	Blade Type	Compactor Shape
Embrittled	Elongated	Gull-Wing
Embrittled	Sharkstooth	Gull-Wing
Embrittled	Elongated	M-Shape
Embrittled	Sharkstooth	M-Shape
Ductile	Elongated	Gull-Wing
Ductile	Sharkstooth	Gull-Wing
Ductile	Elongated	M-Shape
Ductile	Sharkstooth	M-Shape
Ductile	Chisel-Point	Gull-Wing

Figures 3-6 and 3-7 are photos of the product obtained from one of the three shear cuts from each of these combinations, with the piece at the left end of each row being the terminal piece of each specimen. The rows are arranged in the order of decreasing size fraction, in the order: (1) terminal piece, (2) pieces of 1/8-in.-thick stainless steel wrapper, (3) 217 pieces of porcelain-filled tubes, (4) 217 pieces of 55-mil-diam spacer wires, and (5) sieve-classified fines, ranging in size from -4, +10 mesh to -325 mesh. Some general observations to be made from these photos are: (1) the terminal pieces of all embrittled specimens are fractured in at least two locations; (2) there is a wide variation in the length and number of pieces of stainless steel wrapper; (3) several fuel pin fragments are contained in the long pieces of wrapper; and (4) the fraction of fines in each column are generally about equal, with the notable exception of the very small amount of -325 mesh material in the last row of Fig. 3-7.

A plot of the size distribution of the fines produced from shearing is given in Fig. 3-8. All of the fines from each individual shearing operation were classified in a sieve shaker. Sieve Nos. 4, 10, 16, 20, and 30 were used for 20 min of sieving. The -30 mesh material was then transferred to sieve Nos. 50, 100, 200, and 325 for 20 more min of screening.

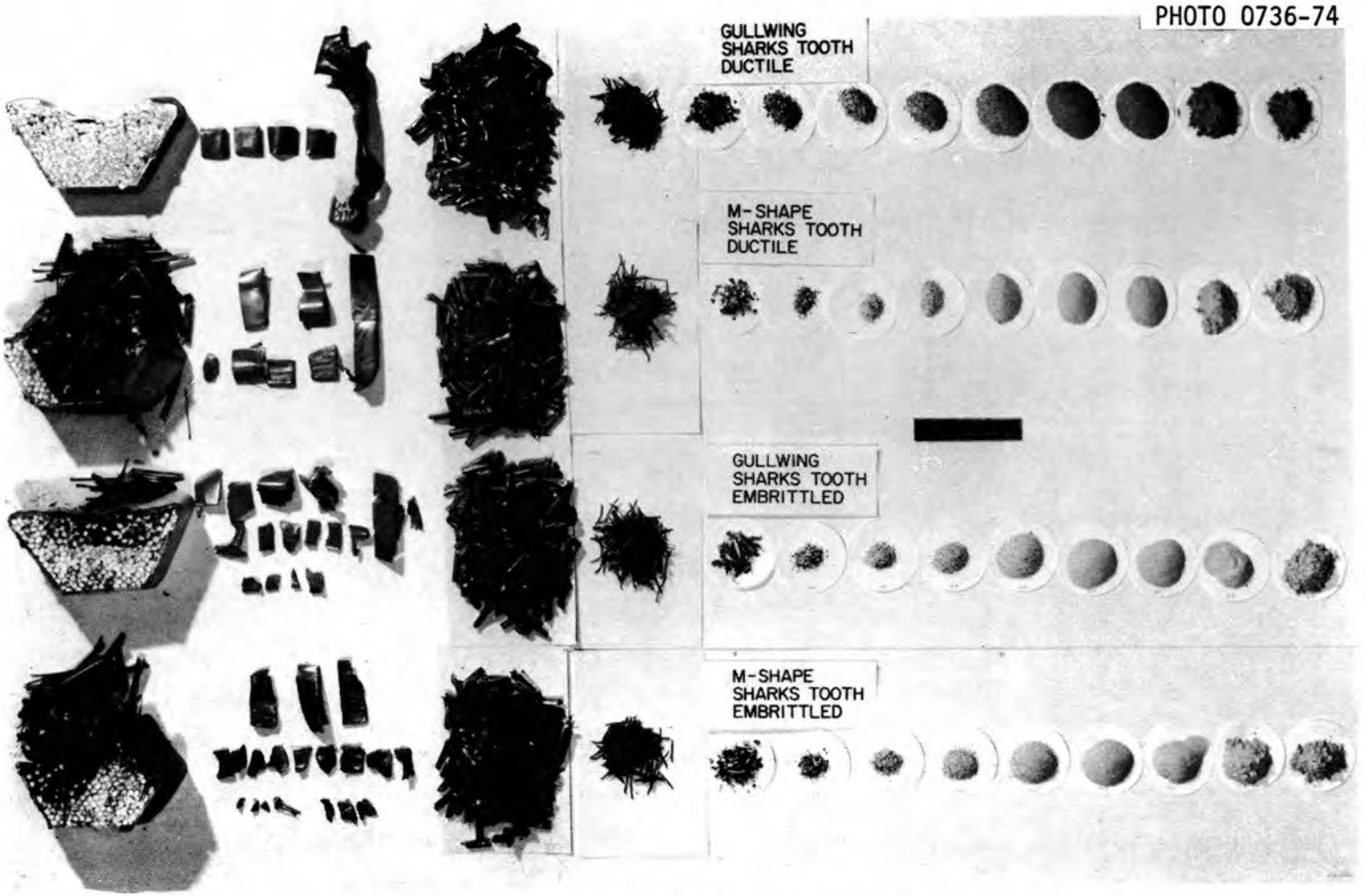

Fig. 3-6. Sheared Prototype LMFBR Fuel.

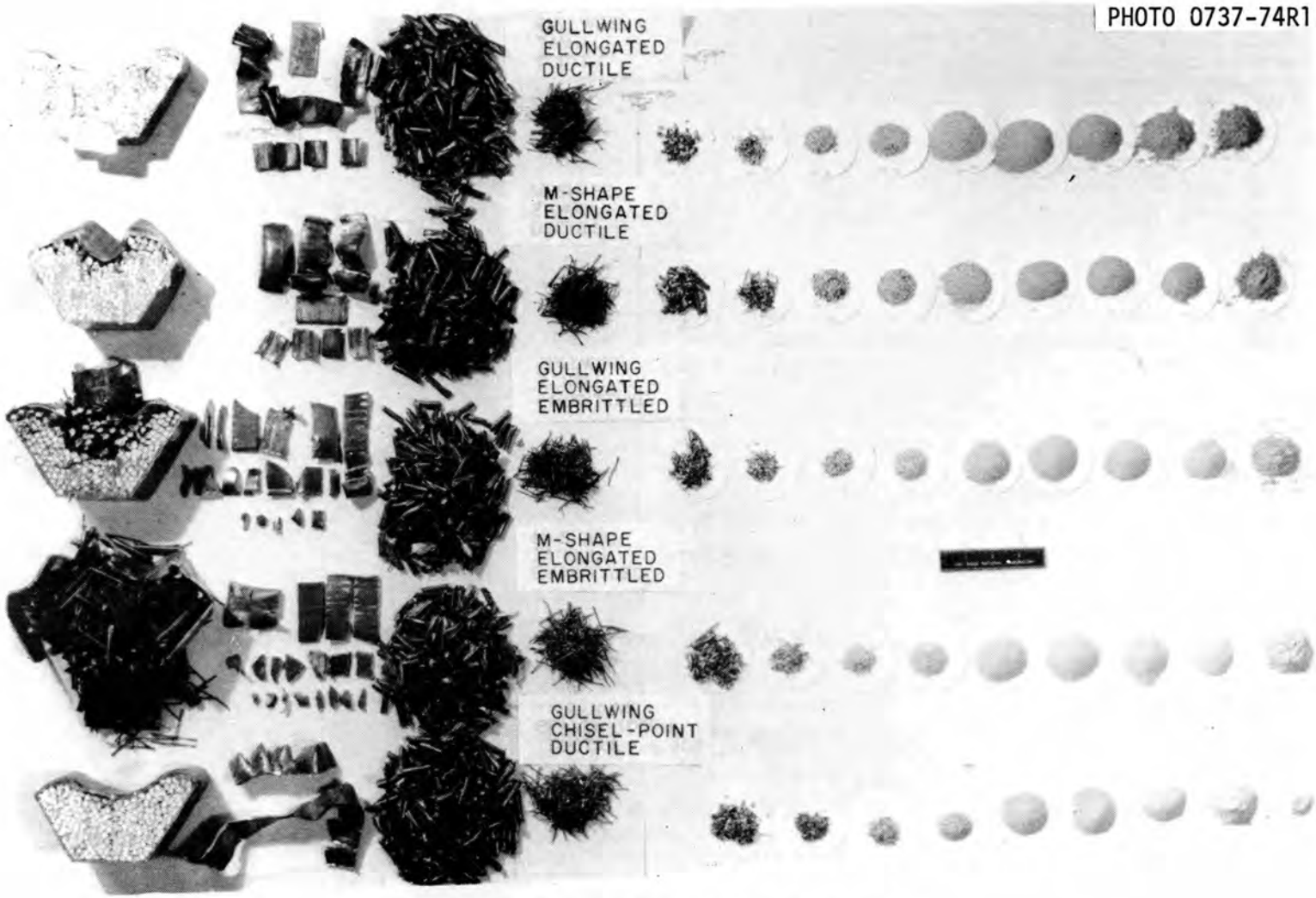

Fig. 3-7. Sheared Prototype LMFBR Fuel.

ORNL DWG 74-2975 R1

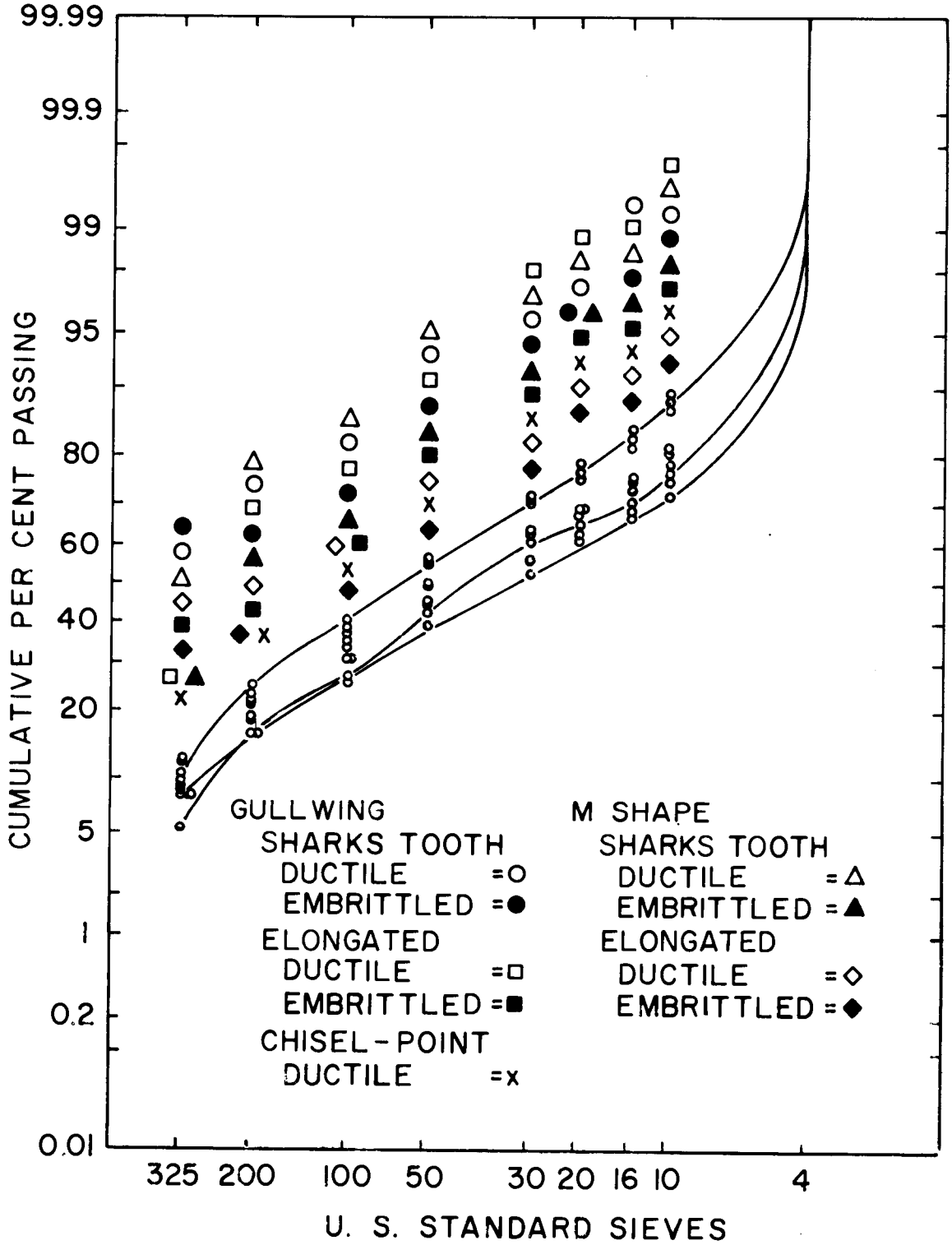

Fig. 3-8. Size Distribution of Fines Generated from Shearing.

The fragments of 1/8-in.-thick stainless steel wrapper were counted and sized in 1/2-in. increments. Histograms of the size distributions obtained from measurements on the total number of pieces obtained in three shearing cuts are shown in Fig. 3-9. Also indicated on the abscissa is the average length of wrapper piece, obtained by dividing the wrapper perimeter by the average number of fragments produced. The size distributions range from the very skewed distributions obtained with ductile stainless steel and the sharkstooth blade, to fairly uniform distributions with the embrittled specimens. The performance of the elongated blade on the ductile specimens is clearly superior to that of the sharkstooth blade, in terms of minimizing the length of fragments. On this same basis, it appears that the M-shape compactor performed better than did the gull-wing with the ductile material. This is probably due to the shorter radius bends in the wrapper obtained with the M-shape compactor. However, these short-radius bends tend to fracture the embrittled stainless steel wrapper excessively during compaction. This fracturing of the wrapper before shearing has occurred will most probably present a problem in feeding the subassemblies to the shear, since uncontained fragments may hamper the operation of the compactor.

The large stresses generated during shearing at points of contact between the fuel pins and the spacer wires tend to split or crack the sheared pins. This tends to expose more of the fuel surface to the dissolvent and can reduce the total dissolution time. Each of the individual sheared fuel pins was examined for evidence of cracking. For the sake of consistency, a split hull was defined as one which was cracked at least 1/2 of its length, or had a hole of any size in it. A plot of the percentage of split hulls determined for each combination of conditions is given in Fig. 3-10. It may be seen that in all cases, the M-shape compactor produced a larger proportion of split hulls than did the gull-wing compactor. The embrittled material also resulted in more split hulls, as may be expected.

3.5 Internal Sodium Removal (Task 3.5)

(S. D. Clinton and J. C. Rose)

A study has been initiated to test methods to deactivate sodium that has leaked into defective LMFBR fuel rods to prevent sodium metal from entering the fuel reprocessing plant dissolver. The contact of nitric acid with fuel and sodium should be avoided because oxide fuel reactions produce oxides of nitrogen while sodium-water reactions produce hydrogen. Mixtures of hydrogen and nitric oxide (NO) are not considered explosive, since the autoignition temperature is greater than 1300°C. At this temperature, the NO decomposes to N_2O and O_2. Mixtures of hydrogen and nitrous oxide (N_2O) are explosive over the composition range of 22-60% H_2 with an autoignition temperature ranging between 670 and 830°C. Hydrogen-nitrogen dioxide (NO_2) mixtures are explosive in the composition range of 30 to 80% H_2 with an autoignition temperature of about 450°C at atmospheric pressure.[2] For a comparison of the potential

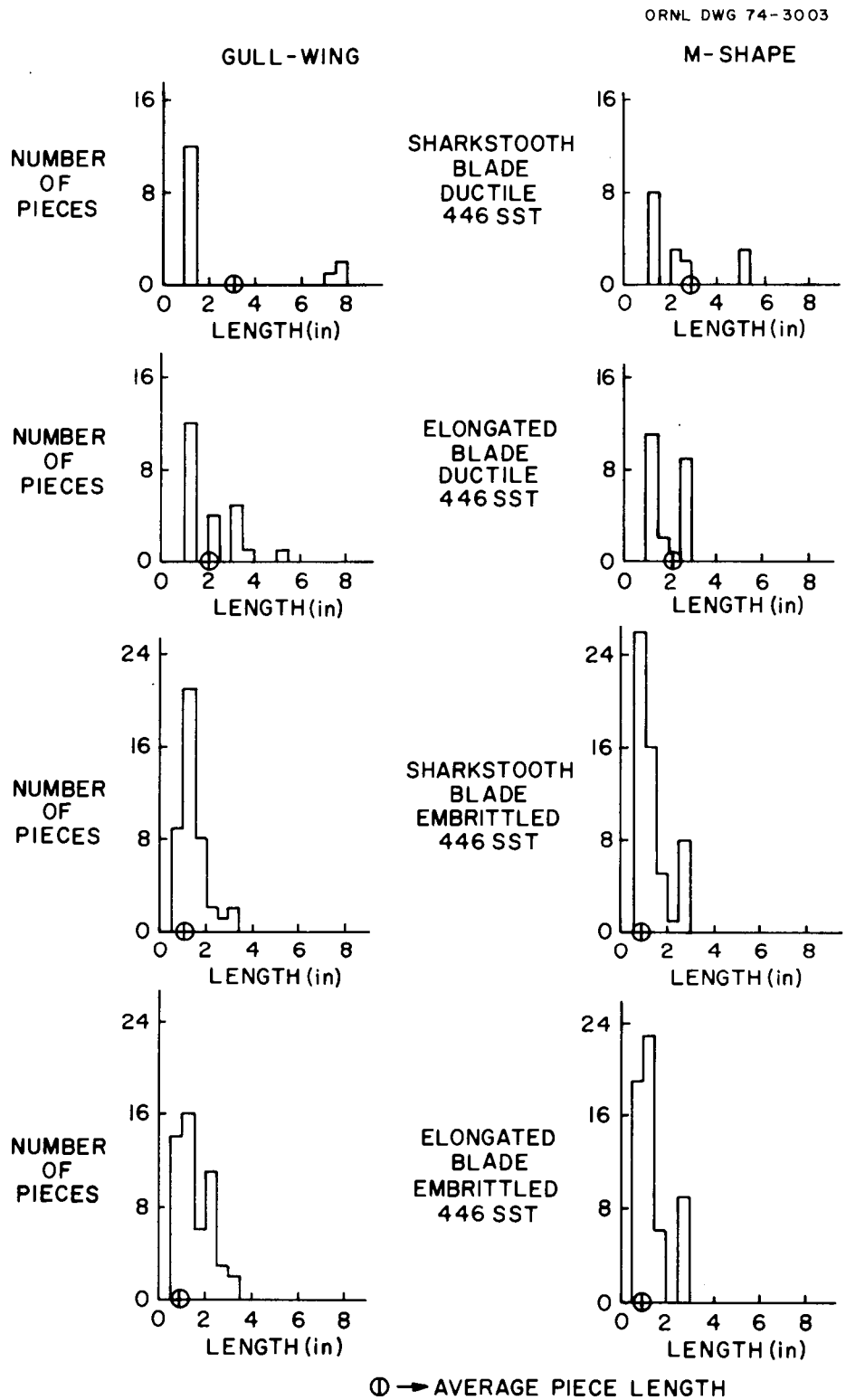

Fig. 3-9. Size Distribution of 1/8-in.-thick Stainless Steel Wrappers Generated from Shearing.

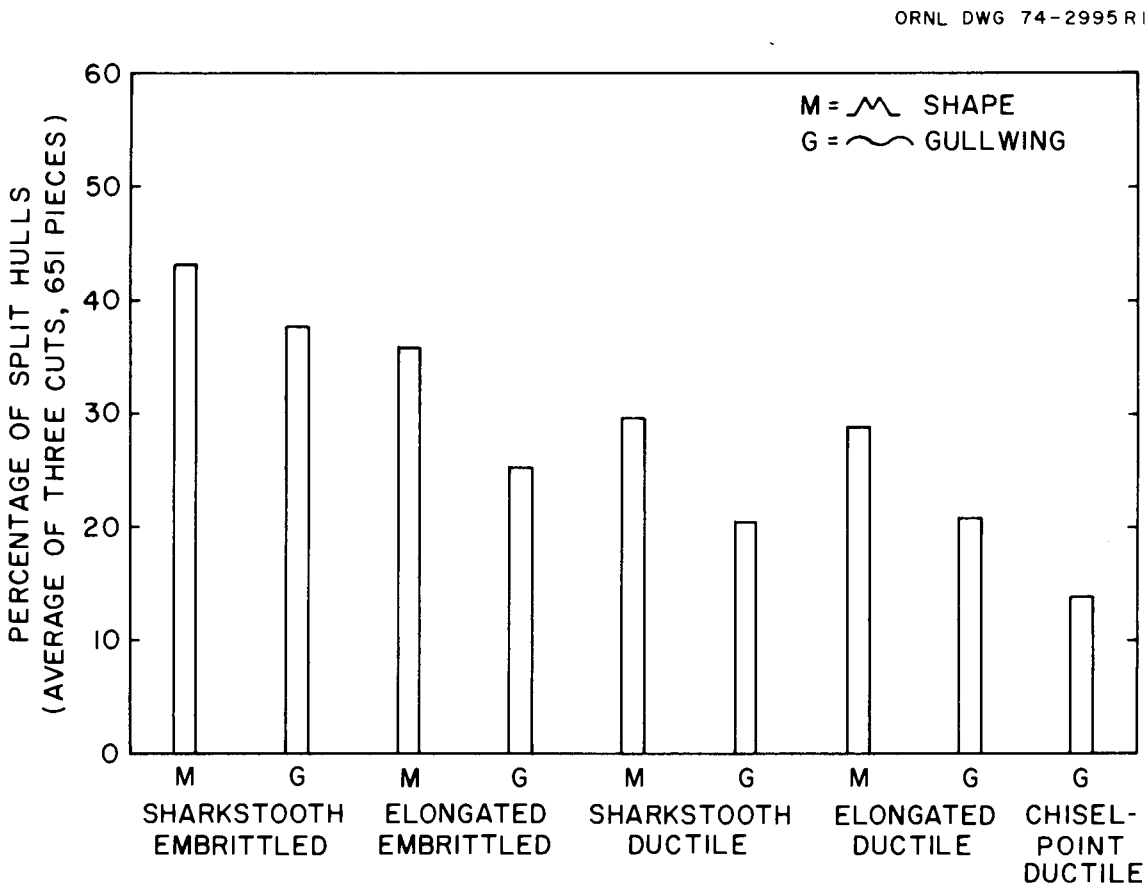

Fig. 3-10. Comparison of Fraction of Split Fuel Pins for Various Shearing Combinations.

hazards, explosive conditions are achieved in hydrogen-oxygen mixtures between hydrogen concentrations of 15 and 90% with an autoignition temperature of about 530 to 560°C. The presence of nitric oxide can catalyze the ignition of hydrogen-oxygen mixtures reducing the autoignition temperature to 380°C. The highly exothermic reaction of sodium and water can be expected to heat metallic sodium beyond the autoignition temperature of gas mixtures and initiate explosions. The unknown is the fact that only certain critical volumes and geometries of gases are explosive and these may or may not be achieved with fuel submerged under a liquid.

A single AI Follow-On fuel rod containing core and axial blanket oxide with the gas plenum removed can be logged with 2 to 6 g of internal sodium (approximately 0.03 to 0.1 g Na/in.). The smaller sodium weight is based on a 2.5-mil annular volume, whereas the larger weight also allows for complete filling of the pellet void volume. For an assumed 1% rod failure, the quantity of sodium to be deactivated per fuel assembly (118 kg U and Pu) is 4 to 12 g. The gas plenums will be removed and isolated from the fueled rods, so that any sodium associated with the gas plenum tubes can be handled separately (about 30 g of sodium per defective rod).

If voloxidation is maintained as an LMFBR fuel reprocessing step, the internal sodium contained in leaking fuel rods can be successfully deactivated by reaction with oxygen. In this instance, the sodium would most probably enter the dissolver as sodium diuranate. If voloxidation is not used as a fuel reprocessing step, the internal sodium could be deactivated by reaction with water in an inert atmosphere (probably nitrogen). A possible problem with this technique is the torturous reaction path which will be available between the cladding and oxide pellets (2- to 3-mil gap). This technique has been demonstrated on 1-in.-diam, 11-in. fuel lengths where the sodium annular thickness was 36 mils.[3]

Before designing engineering scale equipment, the process will be demonstrated on single, 1-in.-long sheared specimens containing annular sodium and urania pellets. The objective will be to keep the sodium deactivation step simple and, if possible, to eliminate the need for a special piece of equipment between the shear and dissolver. Ideally, the internal sodium deactivation should be achieved during the normal transport of sheared fuel between the shearing and dissolution steps. If deactivation of the sodium with water proves unfeasible, then backup methods would include voloxidation (as presently conceived in a rotary calciner) and distillation (HEDL has successfully removed internal sodium from 1-in. lengths in 15 min with helium sweep gas at 0.5 atm and 700°C).[4]

A cylindrical glass vessel (1600-ml volume) is being used to study the reaction rate of water (200 ml) and stainless steel-clad urania pellets containing annular sodium. The prototype fuel specimen (0.305-in.-OD by 0.015-in.-wall tubing filled with 0.270-in.-OD urania pellets)

were sheared into 1-in. lengths and stored in an argon atmosphere.[5] The amount of sodium in each 1-in. sheared length (16 pieces evaluated) varied from 0.030 to 0.060 g. The temperature of the reaction vessel is controlled with a surrounding water bath, and the pressure is continuously recorded by a MKS Baratron pressure meter. For each mole of sodium reacted with water, one-half of a mole of hydrogen is produced; consequently at 20°C, the pressure of the reaction vessel increases about 22 mm Hg per 0.1 g of sodium deactivated.

Twelve runs were made with the sodium deactivation system at 20°C. After purging the reaction vessel with argon, the system is closed, and the sheared prototype fuel is plunged into the water by means of a wire basket and metal rod extending through the rubber stopper seal. The amount of sodium metal reacted is determined from the increase in pressure with time, and the total quantity of sodium present as metal and oxide is found by titrating the alkalinity of the final solution. About 15 to 30% of the annular sodium had apparently oxidized during storage of the sheared pieces (20 months). The results (see Table 3-2) are based on a single 1-in. length of prototype fuel (runs 2, 3, and 4 contained up to three 1-in. sheared lengths). The maximum sodium reaction rates at 20°C varied from 0.5 to 3.3 mg Na/min corresponding to respective mass fluxes of 0.0003 to 0.0020 g/cm^2-sec (based on total annular area of 0.0276 cm^2). The peak reaction rate would generally persist for 10 to 30 min; however, this time period occurred at the beginning in only four of the 12 runs. During the peak reaction rate small hydrogen bubbles (about 1 mm in diameter) could be seen rising continuously from either one or both ends of the fuel piece. The time for complete reaction varied from 24 to 300 min, and apparently during a considerable amount of the run time, the water could not contact the sodium metal due to reaction products or restrictions between the fractured pellets and cladding. Typical annular sodium-water reaction data at 20°C for sheared prototype fuel are shown in Fig. 3-11.

In the immediate future, similar sodium-water reaction data will be obtained on sheared prototype fuel at temperatures up to 95°C.

Table 3-2. Results of Annular Sodium-Water Reactions at 20°C for Single Sheared Lengths of Prototype Fuel

Run No.	Weight of Sodium Reacted (g)	Weight of Sodium Titrated (g)	Fraction of Total Sodium as Metal	Maximum Reaction Rate (mg Na/min)	Maximum Mass Flux (g/cm^2-sec)	Time Period for Maximum Rate (min)	Time for Complete Reaction (min)
1	0.047	0.058	0.81	3.3	0.0020	10-23	24
2[a]	0.024	0.030	0.80	0.5	0.0003	0-29	300
3[a]	0.040	0.053	0.75	3.0	0.0018	19-25	37
4[b]	0.031	0.047	0.66	1.2	0.0008	0-11	60
5	0.045	0.058	0.78	2.4	0.0014	85-93	130
6	0.033	0.048	0.69	0.8	0.0005	46-58	180
7	0.035	0.046	0.76	1.5	0.0009	0-24	24
8	0.037	0.050	0.74	0.9	0.0006	6-38	48
9	0.048	0.055	0.87	2.0	0.0012	12-22	40
10	0.039	0.047	0.83	2.2	0.0013	16-26	30
11	0.042	0.051	0.82	1.3	0.0008	0-18	44
12	0.039	0.050	0.78	1.3	0.0008	34-44	54

Sheared length = 1 in.; clad ID = 0.275 in.; urania pellet OD = 0.270 in.; both ends open.

[a]Two sheared lengths; weight of sodium and reaction rate have been divided by 2.

[b]Three sheared lengths; weight of sodium and reaction rate have been divided by 3.

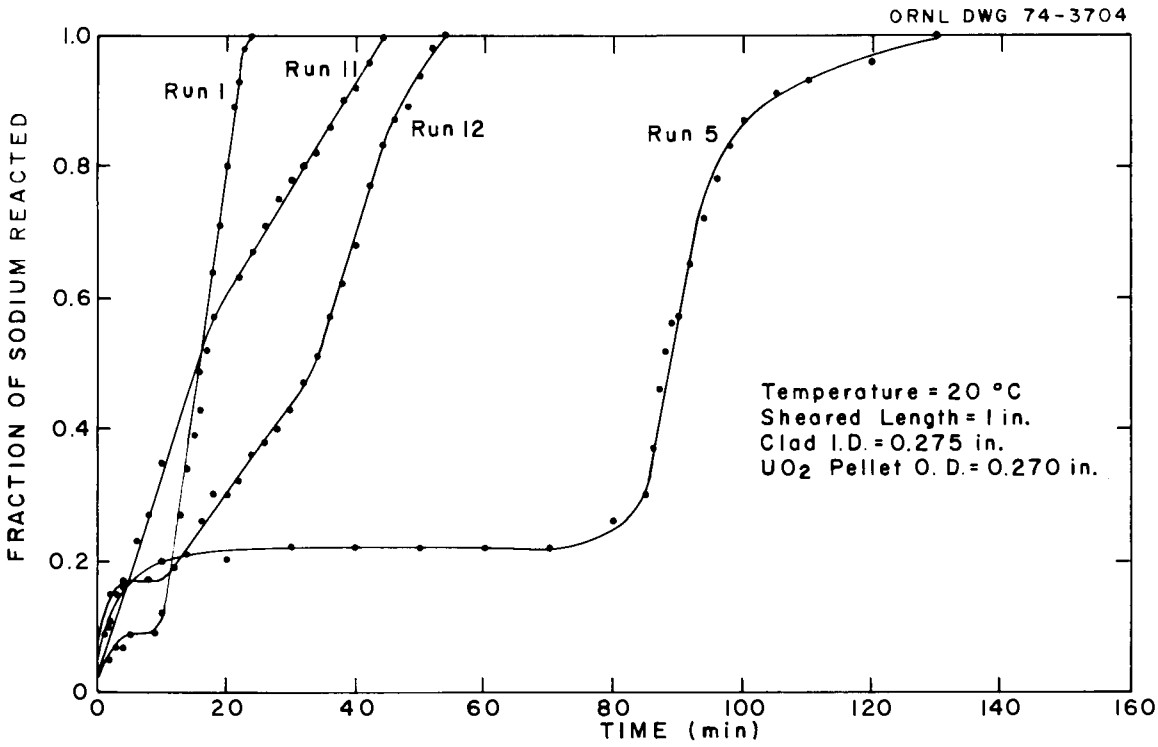

Fig. 3-11. Fraction of Annular Sodium Reacted with Water as a Function of Time.

References for Section 3

1. Aqueous Fuel Reprocessing Quarterly Report for Period Ending September 30, 1973, ORNL-TM-4394 (February 1974)

2. J. E. Johnson, Jr., H_2-O_2-NO_x Flammability and Explosibility: A Literature Survey, ICP-1002, (Oct. 1971).

3. G. P. Miller, Aqueous Removal of Sodium Bond from Unirradiated Hallam Fuel Elements, NLCO-1069, May 1970.

4. J. G. Bradley, Hanford Engineering Development Laboratory, personal communication, January 1973.

5. W. E. Unger et al., LMFBR Fuel Cycle Studies Progress Report for July 1972, No. 41, Sect. 3.3, ORNL-TM-3952.

4. VOLATILE FISSION PRODUCT REMOVAL (TASK 4)

(V. C. A. Vaughen and C. D. Watson)

The objective of Task 4 is to develop a head-end processing method for removing tritium from the fuel prior to aqueous processing. Based on experimental work, it appears that this objective can be met by heating the oxide fuel to about 600°C in flowing oxygen or air (this treatment is termed voloxidation). Early removal of tritium from the fuel into a relatively small volume of gas is desirable to avoid large dilution of the tritium with water in the fuel dissolution step. In addition, the oxidation treatment has the advantage of converting any residual sodium in the fuel to the oxide prior to dissolution.

The first series of voloxidizer optimization studies with HEDL PNL-X-7 fuel yielded the interesting information that the amount of residual tritium after voloxidation appears to be highly dependent on the sample position in the fuel rod.

4.1 Voloxidation from Oxide Fuels (Task 4.1)

(J. H. Goode and O. L. Kirkland)

Hot Cell Studies. - We reported last quarter[1] that about 10% more of the total tritium was released from fuel that had been tumbled during voloxidation than from fuel that had been voloxidized with air passing through a quiescent bed. We designed and carried out a 2^3 factorial experiment to examine the effects of temperature, time, and speed of rotation of the voloxidizer as part of our continuing program to optimize the voloxidizer conditions.

We used segments from PNL-X-7 (HEDL) sheared to about 0.5 inches long. The fuel was made from mechanically blended $(U_{0.75}Pu_{0.25})O_2$ sintered pellets and was irradiated in EBR-II to an average burnup of 7500 MWd/ton (B.U.) and an average linear heat rating (LHR) of 9.4 kW/ft. Using these values and the burnup distribution curve (Fig. 4-1) we calculated the segment burnups, linear heat ratings, and estimated the tritium concentration in the fuel, as determined by a linear relationship between measured tritium content and local/average burnup curves (Table 4-1). Theoretical yields of tritium were 7.26×10^8 and 5.99×10^8 dpm/g $(U,Pu)O_2$ for samples 169 and 178, respectively.

The conditions for the 2^3 factorial experiment were:

	Temperature	Time (h)	Rotational Speed (rpm)
High level	650	4	12
Low level	550	2	6

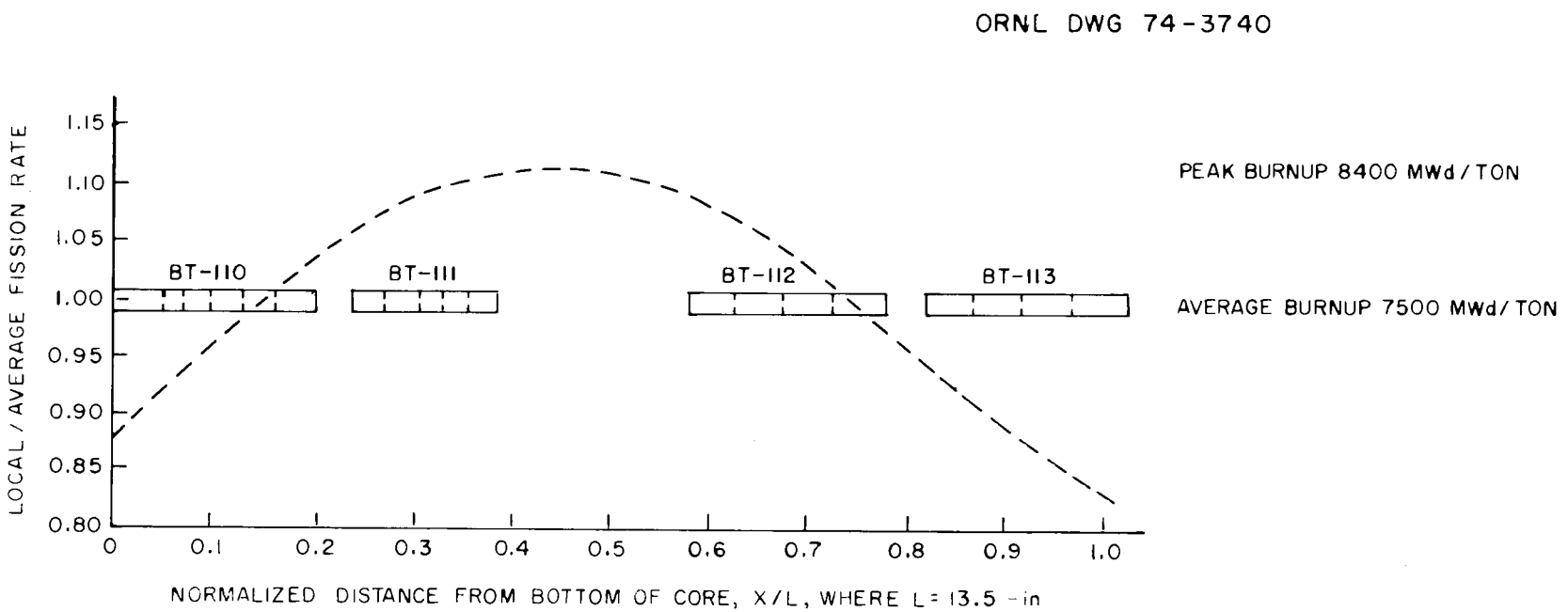

Fig. 4-1. Axial Distribution of Unperturbed Local-to-Average Fission Rates for ^{235}U and ^{239}Pu in the EBR-II Core and Sectioning Diagram for PNL X-7 Fuel Rod.

Table 4-1. Tritium Contents and Linear Heat Ratings of Segments of Rod PNL-X-7

Run No.	Fuel Segment	Local/Avg. Fission Rate	Segment Tritium Content, d/m/mg Pu Measured	Calculated[a]	Linear Heat Rating kW/ft calc[b]
169	111	1.11	3.892×10^4		10.4
170	111	1.10, 1.09		3.690×10^4	10.2
171	111	1.08	-	3.488×10^4	10.1
172	111	1.06	-	3.219×10^4	9.9
173	112	1.06	-	3.219×10^4	9.9
174	112	1.08	-	3.488×10^4	10.1
175	112	1.03	-	2.815×10^4	9.6
176	112	1.00	-	2.411×10^4	9.3
177	113	0.93	-	1.468×10^4	8.7
178	113	0.90	1.064×10^4	-	8.4

[a]Calculated from local-to-average fission rate ratios and measured tritium releases by dissolution.
[b]Calculated from local to average fission rate ratios and average linear heat rating.

The residual tritium was determined from the leach solutions (Section 5.1) and was normalized to the plutonium concentration to adjust for variations in sample weights.

The results are given in Table 4-2 with apparent removals ranging from a low of 96% to a high of 99.98%. Fitting these values into the pictorial form of the 2^3 design (Fig. 4-2) it is immediately apparent that the experimental results were influenced strongly by a fourth variable, which was not randomly distributed throughout the design: namely, fuel segment number. Actually, the effect is probably due to the linear heat rating, although this variable is not independent of the burnup. The speed of rotation of 6 rpm or 12 rpm for 2 to 4 hours is probably a minor variable, and the sample number was substituted (Fig. 4-3). This design is incomplete. However, one can determine some trends. The strongest trend is that of fuel segment number, showing a strongly decreasing residual tritium content with segment numbers; 111 > 112 > 113. This is the same order as decreasing average linear heat rating (burnup?); 10.2 > 9.7 > 8.7 kW/ft. There are not enough data to determine the significance of the time or temperature dependences, although both appear negative - i.e., longer voloxidation time → less residual tritium; higher temperature → less residual tritium.

Table 4-2. Determination of Effects of Time, Temperature, and Speed of Rotation on Volatilization of Tritium

Exp. No.	Fuel Description - PNL-X-7				Temp., °C	Time-hr	rpm	Tritium Content - dpm/mg Pu		
	Segment BT	Calc. LHR	Total-g	Fuel-g				Initial (calc.)	Final (meas.)	% Remaining (calc.)
169	111	10.4	6.10	3.88	-	None	-	38,900	-	100
178	113	8.5	4.45	3.41	-	None	-	10,640	-	100
174	112	10.2	5.91	3.59	550	2	6	34,890	281	0.80
173	112	10.0	4.45	3.42	550	2	12	32,190	243	0.79
175	112	9.7	4.54	3.33	650	2	6	28,150	< 10	< 0.04
171	111	10.2	4.87	4.03	650	2	12	34,890	1394	4.00
177	113	8.7	5.63	3.12	550	4	6	14,680	15	0.10
170	111	10.3	7.59	4.52	550	4	12	36,910	1368	3.71
172	111	10.0	3.85	1.86	650	4	6	32,190	38	0.12
176	112	9.4	7.09	4.47	650	4	12	24,110	< 5	< 0.02

ORNL DWG 74-3741

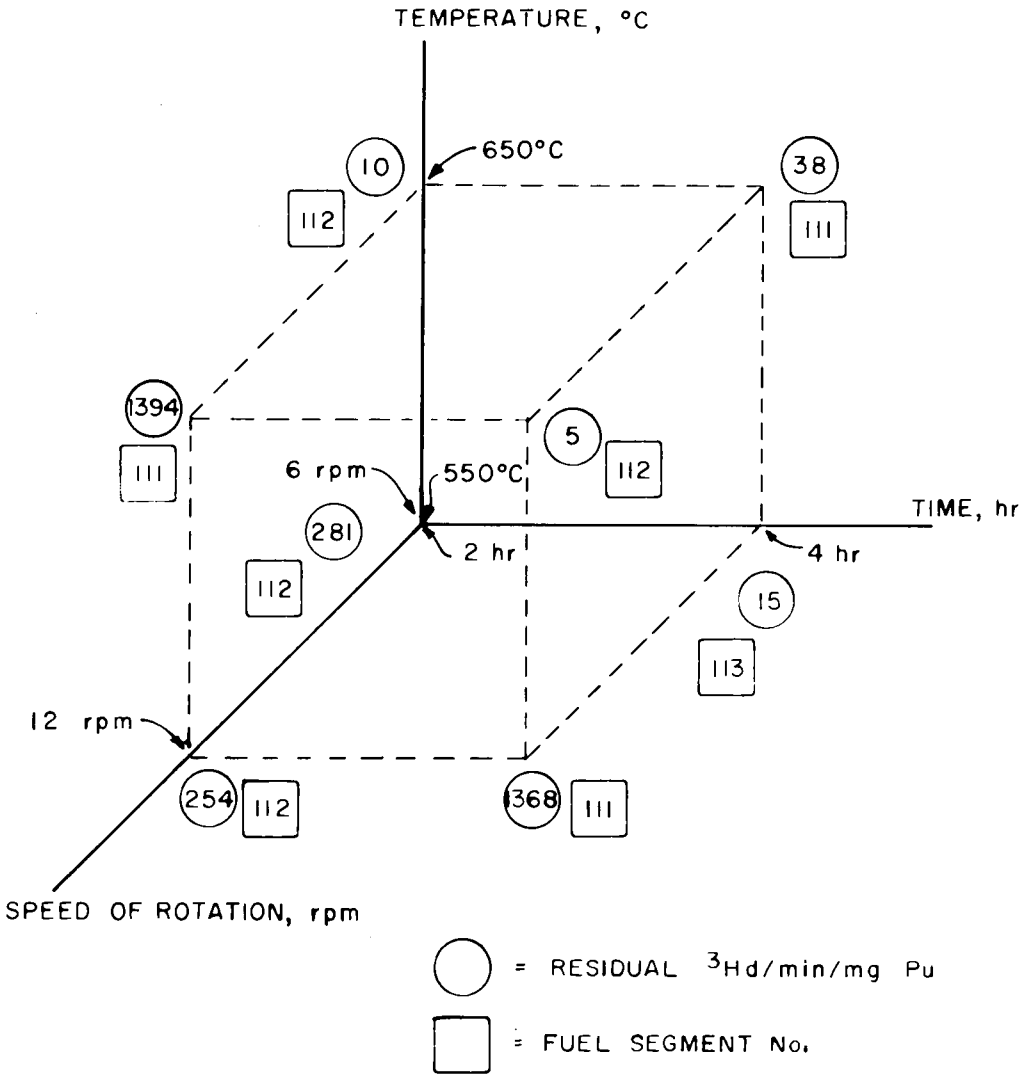

Fig. 4-2. 2^3 Experimental Design (Original) for Time of Voloxidation, Temperature of Voloxidation, and Speed of Voloxidizer Rotation.

ORNL DWG 74-3742

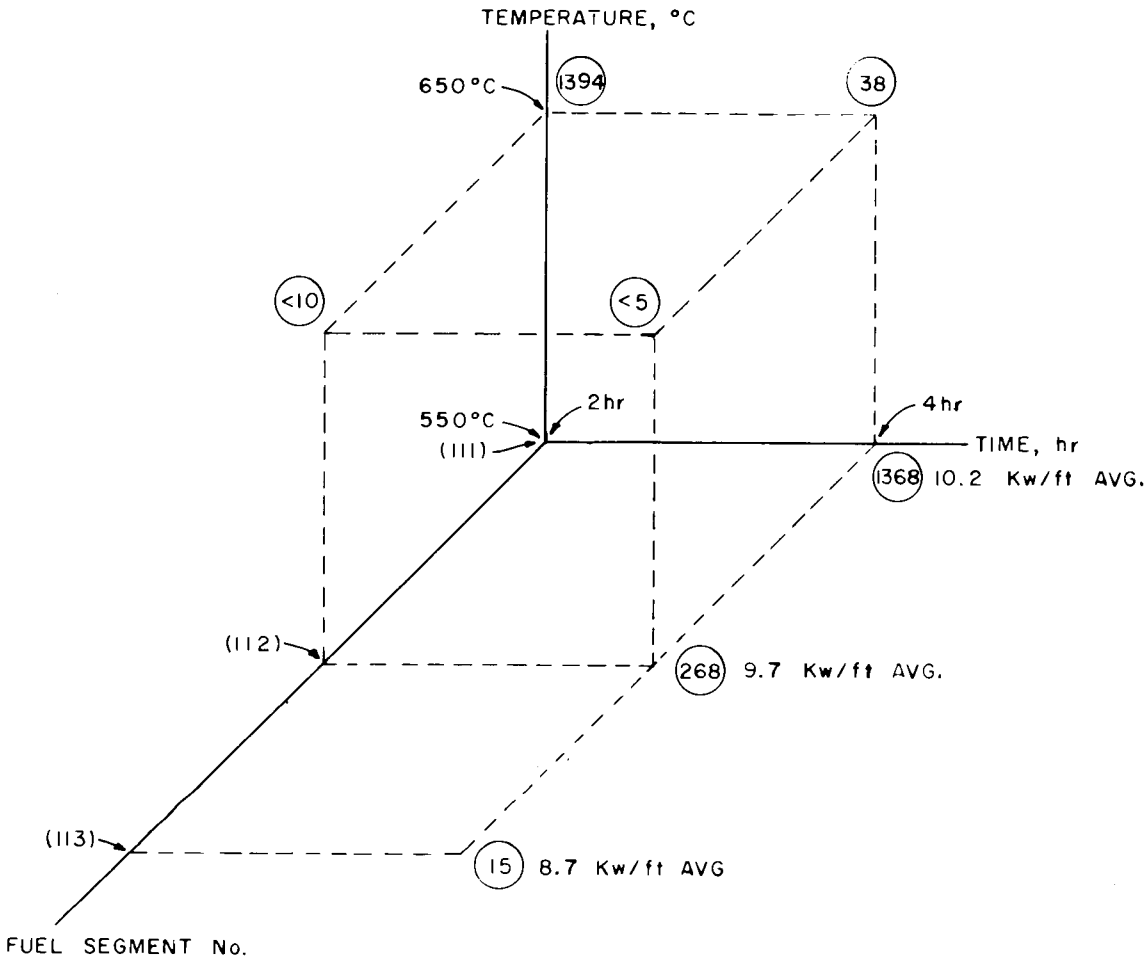

NOTE: DATA FROM Fig. 4-1 USED; ASSUMED SPEED OF ROTATION EFFECT = 0. SUBSTITUTED FUEL SEGMENT No. DESIGN INCOMPLETELY TESTED.

Fig. 4-3. Rearranged 2^3 Experimental Design (Incomplete) for Temperature of Voloxidation, Time of Voloxidation, and Fuel Sample Number. Circled numbers = 34 d/m/mg Pu in solution (residual tritium values).

To avoid this fine scale variation, it will be necessary to homogenize and subdivide the fuel from each individual rod or test series into random samples before running future optimization studies. This procedure will also more nearly simulate actual voloxidizer operations in a real plant where whole fuel assemblies will be reprocessed.

Reference for Sect. 4

1. W. E. Unger *et al.*, Aqueous Fuel Reprocessing Quarterly Progress Report for Period Ending Dec. 31, 1973, ORNL-TM-4488 (1974).

5. DISSOLUTION (TASK 5)

(V. C. A. Vaughen and C. D. Watson)

The objective of Task 5 is to ensure that LMFBR fuels can be dissolved in nitric acid with high metal recoveries. Since the dissolution characteristics of the fuels can vary widely, depending on their plutonium content, method of preparation, and irradiation histories, extensive leaching data are being obtained to define the effects of the many variables. A thorough understanding of iodine chemistry in the dissolver system is needed as a guide for providing effective iodine control. The dissolver equipment must be designed and operated within rather narrow limitations imposed by criticality control and off-gas considerations. It appears that satisfactory solution of these problems can best be accomplished using continuous dissolving methods and this approach is being emphasized. Evolution of a successful dissolver will require development of equipment for dependably moving the sheared stainless steel hulls and other solids through the system, and development of seals for isolating the system to prevent excessive inleakage of diluent gases.

5.1 Dissolution of Oxide Fuels (Task 5.1)

(J. H. Goode and O. L. Kirkland)

Hot Cell Dissolution Tests. - We leached the $(U,Pu)O_2$ samples from HEDL experiment PNL-X-7 (Task 4 above) for two one-hour periods in 6 M HNO_3. The concentrations in the dissolver product at the end of the first hour were about 0.5 M (U + Pu) and 3 to 4 M H^+. The solutions were filtered to separate the cladding and insoluble residues for analysis (Table 5-1).

The data indicated there was a small adverse effect (from ∿ 0.01 to ∿ 0.03%) on the amount of residue of PuO_2 in the 6 M HNO_3 due to the increase in the voloxidation temperature from 550° to 650°C for the samples irradiated to ∿ 10 kW/ft. Effects of the speed of voloxidizer rotation and time of voloxidation were not significant.

Residue Characterization. - Two pieces of stainless-clad fuel from segment BT-110 of experiment PNL X-7 (12.23 g) were oxidized by tumbling for 2 hr at 600°C in a 50 cc/min stream of air (about 400% excess O_2); the fuel was dislodged from the cladding. The oxidized fuel was leached for 1 hr in boiling 6 M HNO_3 and the residue was separated from the solution by settling and decantation and washed. Samples of the residue were examined with the scanning electron microscope (SEM) and were used in particle settling rate studies. The settling rate measurements indicated that about 25% of the particles had an apparent diameter of ≥ 40 μm, 50% were ≥ 20 μm, 75% were ≥ 16 μm, and ∿ 90% ≥ 8 μm. SEM photographs of the larger, etched dendrites confirmed the sizes estimated from settling rate data. X-ray fluorescence spectra of the dendrites indicated the larger crystals were principally lead; HEDL has no information as to the source of the lead contamination. A great number of 0.5 to 1.5 μm particles were also photographed; X-ray fluorescence indicated niobium, cerium, and possibly uranium were present. Other analyses are not available at this time.

Table 5-1. Dissolution of PNL X-7 $(U,Pu)O_2$ in Boiling 6 M HNO_3

Run No.	Rod Sample No.	Volox. Temp. (°C)	Undissolved at 1 hr U (%)	Undissolved at 1 hr Pu (%)	Undissolved at 2 hr U (%)	Undissolved at 2 hr Pu (%)	Residue Pu/(U+Pu)
169	111	-	0.24	0.21	0.046	0.004	a
170	111	550	0.18	0.17	0.050	0.012	a
171	111	650	0.58	0.22	0.024	0.055	0.420
172	111	650	0.08	1.25	0.024	0.031	0.262
173	112	550	0.14	0.18	0.006	0.012	0.397
174	112	650	0.04	0.07	0.004	0.004	0.259
175	112	650	0.12	0.17	0.028	0.012	a
176	112	650	0.16	0.25	0.040	0.015	a
177	113	550	0.21	1.22	0.007	0.011	0.318
178	113	-	-	-	0.008	0.013	0.331

[a]Samples being rechecked.
[b]8 M HNO_3--0.05 M HF used as dissolvent.

Effect of Complexing Fluoride Dissolvent. - The beneficial effect of Ce^{4+} as an agent to promote the dissolution of PuO_2 in nitric acid was found to be overcome by the presence of ruthenium, which rapidly and preferentially reduced the ceric ion.[1,2] The use of fluoride in a secondary dissolvent was therefore indicated in order to ensure complete dissolution of plutonia. Horner et al. prepared a quantity of the plutonium-rich residue by dissolving a large batch of FTR Dissolution Reference Pellets in HNO_3.[2] A 141 mg sample of the $(U_{0.2}Pu_{0.8})O_2$ was refluxed in 25 ml of 8 M HNO_3--0.015 M HBF_4 for 1 hr to determine whether the boron complex would affect the dissolution. The presence of the boron had no effect on the dissolution of the plutonia; all but 0.004% of the material dissolved.

Corrosion Tests. - Short-term corrosion tests were made with NIMONIC PE-16, a wrought nickel-chromium-iron base alloy being considered as a material of construction, and with embrittled Type 446 stainless steel, which may be used as a cladding material for the cold engineering demonstration of LMFBR processing. Table 5-2 summarizes the tests. Both materials are relatively resistant to 4-8 M HNO_3, are less so with 12 M HNO_3, and corrode badly (lose nickel) in 8 M HNO_3--0.05 M HF.

Table 5-2. Corrosion of Nickel-Chromium-Iron Base Alloys by Process Solutions.

Process Solution	Length of Test (hr)	Penetration Rate (inches per year) NIMONIC PE-16	Type 446
4 M HNO_3--100 g U/l	72	0.001	-
6 M HNO_3	48	0.0015	-
6 M HNO_3	72	-	0.0024
8 M HNO_3	24	0.002	-
12 M HNO_3	24	0.006	0.007
8 M HNO_3--0.05 M HF	24	0.441	0.041

5.2 PRIMARY DISSOLVER STUDIES (TASK 5.4)

(R. B. Heimdahl and D. A. McWhirter)

The investigation of fluid flow and solids transport problems associated with various primary dissolver concepts was continued. Several additional hull rinsing tests were conducted with the static-bed hull rinsing test loop, using smaller particles than in previous tests as the simulated insoluble material. Hull rinsing studies were also continued with the 12-in.-diam compartmented rotary dissolver, and the design of a large-scale, 48-in.-diam rotary dissolver was continued.

Static-Bed Hull Rinsing Tests. - The purpose of the static-bed hull rinsing tests was to simulate the rinsing or washing of insoluble particles from the stainless steel hulls resulting from the shear-leach reprocessing method.[1] Other studies have indicated that a substantial fraction of the PuO_2 in the mechanically blended UO_2-PuO_2 fuels is essentially insoluble in HNO_3. It is highly desirable from economic and criticality considerations to recover these insoluble fractions. The proposed manner of recovery is to remove these insoluble particles from the stainless steel hulls and transfer them to a more corrosive medium in a secondary dissolver.

As previously reported,[1] several hull rinsing tests were conducted using -325 mesh (44 μm) nickel and lead particles to simulate the insoluble fines occurring during the dissolution of LMFBR fuel. Since that time, a better characterization of the undissolved residue indicates a size distribution where 50% of the particles range in size from 8 to 20 μm, and 50% range from 3 to 8 μm. To better simulate the rinsing characteristics of the smaller particles, additional rinsing tests were conducted using 4 to 7 μm nickel particles, and 2.2 to 3.0 μm nickel particles, as the simulated insoluble residue. The 4 to 7 μm particles are nearly spherical, with small surface protrusions making them appear to be clusters of smaller particles. The 2.2 to 3.0 μm nickel particles are elongated and irregular in shape.

Basically, the rinse procedure was to add a measured mass of the nickel powder to the 4-in.-diameter column containing 1-in.-long, 1/4-in.-diam stainless steel hulls and water. This was followed by a 2 to 4 hr period of downflow through the column at a water flow rate of 0.75 liters/min. The column was then drained and refilled three times using a drain rate of 4 ft/min and a fill rate of 1 ft/min. The nickel remaining in the column was then dissolved in HNO_3 and the solution analyzed for its nickel content. This allowed the rinse efficiency to be calculated from the relationship:

$$\text{Eff } (\%) = [1 - \frac{M_f}{M_i}] \times 100$$

where

M_f = mass of nickel remaining in column and

M_i = mass of nickel added to column.

Table 5-3 indicates the rinse efficiencies determined from the recent tests. These results are comparable to the results obtained with the -325 mesh nickel particles,[1] which had an average size of ∿ 35 μm. Thus, apparently there is very little difference in the rinsing characteristics of particles ranging in size from ∿ 40 μm to ∿ 2.5 μm, in a static bed of hulls.

Table 5-3. Rinse Efficiencies from Static Bed Tests.

Test Number	Particles Used	Rinse Efficiency (%)
SB8	4-7 μm nickel	8.6
SB9	4-7 μm nickel	12.6
SB10	4-7 μm nickel	12.6
SB11	2.2-3.0 μm nickel	21.4

That they were not effectively removed from the column indicates that the static bed of stainless steel hulls tended to trap the particles, either internally or by deposition at stagnation points.

Rotary Dissolver Hull Rinsing Tests. - Hull rinsing tests were continued with the 12-in.-diam compartmented rotary dissolver. The backmixing problem, previously reported, has been eliminated by sealing the annular clearance between the drum walls and the periphery of the bulkheads with a silicone sealant, along with the previously reported modifications. Several more hull rinsing tests were conducted using this unit. The liquid level in the 12-in.-diam. drum was reduced to an operating level of 1.5 to 2.0 in. by the installation of a dip leg coupled to the suction side of a centrifugal pump. Previously, an overflow line at the 4-in. level was used. The method of testing was to add measured amounts of either lead or nickel particles and ∿ 1/2 kg of empty stainless steel hulls to the loading compartment of the rotary unit. A countercurrent flow of rinse water was established, and after the desired rinsing time in one stage was attained the hulls were advanced to the next stage and another batch was loaded into the loading compartment. Generally, 3 or 4 batches were transferred through the dissolver in a given rinse test. The rinse efficiency was found by leaching the rinsed hulls in HNO_3 and analyzing the resulting solution for its lead or nickel content.

An average of the rinse efficiencies determined in 11 tests in which nickel particles were used as the simulated insoluble particles indicates a rinse efficiency of 99.92%. There was very little effect noted when varying the rinse flow rate by a factor of 4 or varying the rinse time per stage from 10 min to 60 min. The range of the rinse efficiencies determined in these 11 tests was from 99.84% to 99.96%. The use of -325 mesh lead particles as the simulated insoluble particles resulted in a lower rinse efficiency for these heavier particles at given conditions of flow rate and time/stage and also a greater range in efficiencies. The range in rinse efficiencies for the seven tests conducted with lead particles was from 99.27% at a flow rate of 0.17 gpm to 99.77% at 0.67 gpm. The expected flow rate to be used in a large-scale 48-in.-diam dissolver corresponds to ∿ 0.3 gpm in the 1/4-scale unit under test, and three tests run with a flow rate of 0.34 gpm yielded an average rinse efficiency of 99.66%. These rinsing tests indicate that with

three stages of rinsing and a nominal time of 30 min per stage, rinsing efficiencies of at least 99.5% may be expected. The effect of adding more stages of rinsing has not been investigated, although it would appear that more stages could only improve on the overall efficiency. Increasing the residence time per stage can also improve the efficiency, as can increasing the rinse liquid flow rate.

Engineering-Scale Rotary Dissolver and Related Equipment. -- The design of a large-scale, 48-in.-diam rotary dissolver was continued. This unit will be used to demonstrate the transport of sheared fuel including pieces of 1/8-in.-thick stainless steel wrapper which result from the shearing of whole fuel subassemblies into 1-in. lengths. It will also be used to check design features necessary to ensure the containment of off-gases during dissolution.

Some design changes have resulted from experience with the 12-in.-diam rotary dissolver, and these will be incorporated into the latest design of the engineering-scale dissolver. The backmixing of fluid, which presented a problem with the small dissolver, can be remedied by installing internal fluid transfer ducts to pump the fluid from one compartment to the next. The use of an internal pumping system to transfer the product solution out of the dissolver will provide a positive flow control without the need for an external pumping system. The inlet and discharge pipes are 12-in.-diam to prevent possible blockages caused by bridging of large pieces of sheared material. The internal solids transfer duct is 20 in. in diam.

The entire unit will be contained within a stainless steel enclosure, thus eliminating the need for large-diameter rotary face seals for off-gas containment. The enclosure penetrations require only static seals, with the exception of a small diameter shaft seal for the drive shaft. A purge gas flow will be provided to ensure an inflow of gas through the annular clearance between the rotating drum and the stationary end sections.

A 24-in.-diam (1/2-scale) model of the solids loading compartment of the engineering-scale rotary dissolver is being fabricated. The interactions between the purge gas inflow and any generated foam or splashing caused by the internal pumping system will be observed with this model which features a transparent window.

A solids conveying system suitable for transporting sheared material from one reprocessing station to another was designed. This system will be tested with the 48-in. dissolver by transporting solids from the dissolver discharge back to the inlet. A belt conveyor is used to carry the solids from the submerged discharge chute of the dissolver to the inlet hopper of a vertical, continuous bucket elevator. The elevator will discharge into a conduit which returns the solids to the dissolver via a double flap isolation valve.

The plans for next quarter's work include experimental investigations with the 1/4-scale and 1/2-scale rotary dissolver models, and continuing the design and fabrication of the engineering-scale dissolver.

The investigations with the 1/4-scale dissolver will be directed toward determining the conditions which may cause the deposition and buildup of solids on the inside surfaces of the rotary dissolver. Closely tied in with this study will be a qualitative investigation of the effects of foaming on the dissolver's operation.

References for Sect. 5

1. W. E. Unger *et al.*, Aqueous Fuel Reprocessing Quarterly Progress Report for Period Ending Dec. 31, 1973, ORNL-TM-4488 (1974).

2. W. E. Unger *et al.*, Aqueous Fuel Reprocessing Quarterly Progress Report for Period Ending Sept. 30, 1973, ORNL-TM-4344 (Feb. 1974).

6. FEED PREPARATION (TASK 6)

(V. C. A. Vaughen)

The aqueous feed discharged from the dissolver will contain solids (undissolved fission products, corrosion products, etc.) and will probably require clarification prior to solvent extraction. Preparation of the feed for solvent extraction also will include adjustment of the plutonium valence and the nitric acid concentration, and a treatment to remove iodine.

There was no reportable progress on this task this month.

7. SOLVENT EXTRACTION (TASK 7)

(V. C. A. Vaughen and C. D. Watson)

The objective of Task 7 is to establish that LMFBR fuels can be processed successfully by solvent extraction methods.

Work on Task 7 has been suspended for FY 1974.

8. PLUTONIUM PURIFICATION (TASK 8)

(V. C. A. Vaughen)

This task covers the process steps in purifying plutonium, starting with the plutonium product solution from the first Purex cycle and continuing through preparation of a product solution of adequate purity and concentration for delivery to the fuel refabrication operation.

Work on Task 8 has been suspended for FY 1974.

9. WASTE TREATMENT AND STORAGE (TASK 9)

Progress on this task is reported separately.

10. OFF-GAS TREATMENT (TASK 10)

(V. C. A. Vaughen, C. D. Watson, O. O. Yarbro)

The development of processes for removal of volatile fission products from gas streams was continued this quarter. Various aspects of the Iodox system for iodine removal and control were further investigated.

10.1 Iodox Process Demonstration

(B. A. Hannaford, D. E. Spangler, W. S. Groenier)

Iodine scrubbing experiments in the seven-plate, 7.6-cm, bubble-cap column were continued and runs BCX-5 and BCX-6 were completed to study the effect of CO_2 on scrubbing efficiency.

The resulting decontamination factors (DFs) indicated that the high CO_2 content would have no effect upon the iodine removal efficiency of the gas scrubbing equipment. The effect of CO and the effect of elemental I_2 as opposed to CH_3I will be tested in the next report period. The results of the two experiments are summarized in Table 10-1 and have been combined with results of earlier bubble-cap experiments in Fig. 10-1. The trend of the DFs beyond the second plate appears to indicate that the performance of additional plates remains unchanged even as the concentration of CH_3I in the gas phase becomes very low. This concentration is calculated to be about 4×10^{-8} mole fraction CH_3I in air leaving the seventh plate in experiments BCX-5 and BCX-6.

10.2 Nitric Acid Production by Extractive Distillation

(B. A. Hannaford, D. E. Spangler, W. S. Groenier)

The requirement for highly concentrated (20 to 22 *M*) nitric acid feed for the Iodox process provides an incentive for incorporating a nitric acid process in the flowsheet which is capable of upgrading dilute nitric acid across the azeotropic concentration of 68.5 wt %. One attractive concentration process utilizes magnesium nitrate as a neutral salt to effectively extract water from the water—nitric acid system. In the simplest form of the process, hot 72 to 74 wt % magnesium nitrate is mixed with room-temperature 13 *M* nitric acid in the proper proportions to yield an equilibrium vapor containing 90 to 95% nitric acid. Our bench-scale work on the process, which was begun in this report period, will be followed by a scaled-up demonstration of the nitric acid process integrated with the Iodox process.

The bench-scale equipment was installed in a walk-in hood in Building 4505 as shown schematically in Fig. 10-2 and as installed in Fig. 10-3. A magnetically-coupled centrifugal pump (P1) recirculates magnesium nitrate solution through a 4.3-ft^2 heat exchanger HX2 where 230-psi steam supplies the heat for evaporating water from the solution at temperatures approaching 190°C for the 74 wt % solution. Condensate is collected for measurement in

Table 10-1. Nitric Acid Scrubbing of ^{131}I-Traced Methyl Iodide from Air and CO_2-Air Streams at 25°C

Flow rate of 20 *M* HNO_3 scrub solution 0.077 liters/min; flow rate of gas 28 liters/min (STP). Bubble-cap column specifications: column diameter 7.6 cm, plate-to-plate spacing (minimum) 15 cm, slot submergence 3 cm, and liquid holdup per plate 0.18 liter. Steady-state run time 60 min.

	BCX-5	BCX-6
Gas composition, inlet	170 ppm CH_3I in Air	170 ppm CH_3I in 92.8% CO_2–7.2% Air
DF, Plate 1	6.3	5.9
2	4.0	3.6
3	2.7	3.0
4	3.0	2.8
5	2.9	3.1
6	2.4	2.5
7	3.1	3.3
Ave.	3.3	3.4
DF, Column	4700	5000
DF, Condenser	13	10
DF, Overall	6×10^4	5×10^4

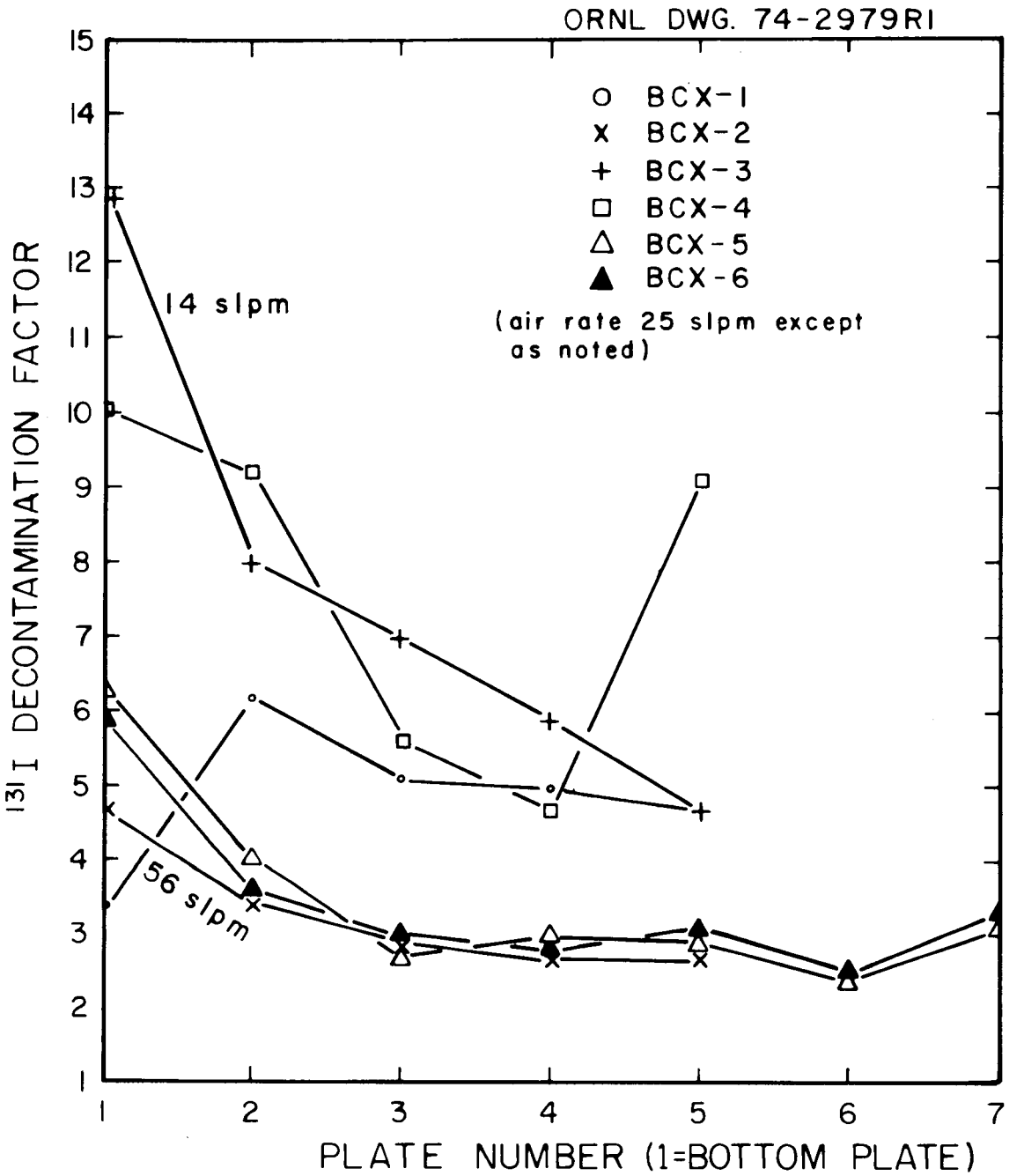

Fig. 10-1. Decontamination Factor for ^{131}I vs Plate for a 7.6-cm-diam Bubble-Cap Column. Methyl iodide contaminant in air, scrubbed with ~ 20 *M* HNO_3 at 25°C (air rate 25 slpm except as noted).

ORNL DWG 74-5500

Item	Description
T1	Feed tank conc. $Mg(NO_3)_2$
T2	Receiving tank, dilute $Mg(NO_3)_2$
T3	Feed tank, dilute HNO_3
T4	Product tank, acid condensate
T5	Receiver, water condensate
T6	Calibration tank for pump P1
C1	Condenser
C2	Condenser
C7	Packed column, 3.8 cm diam x 112 cm long
HX1	Heat exchanger, cooling or heating
HX2	Heat exchanger, heating

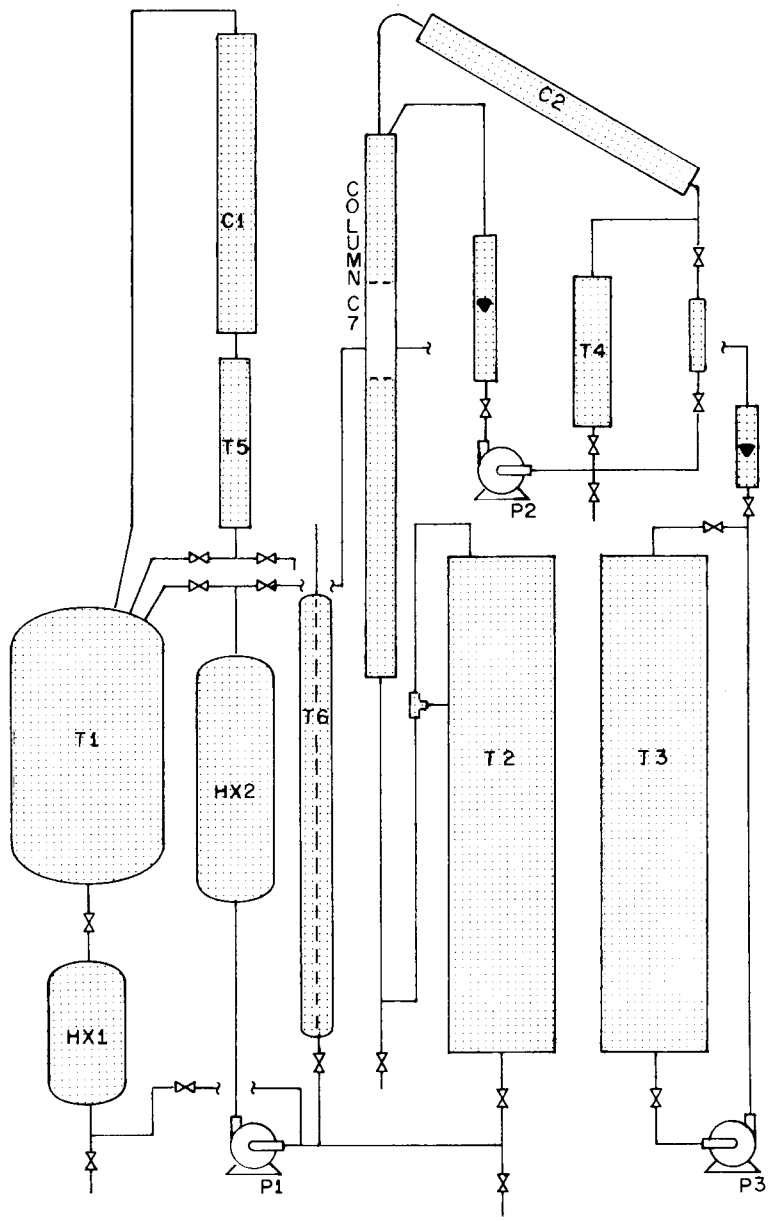

Fig. 10-2. Elevation Sketch of Bench-Scale Equipment for Nitric Acid Production by Extractive Distillation.

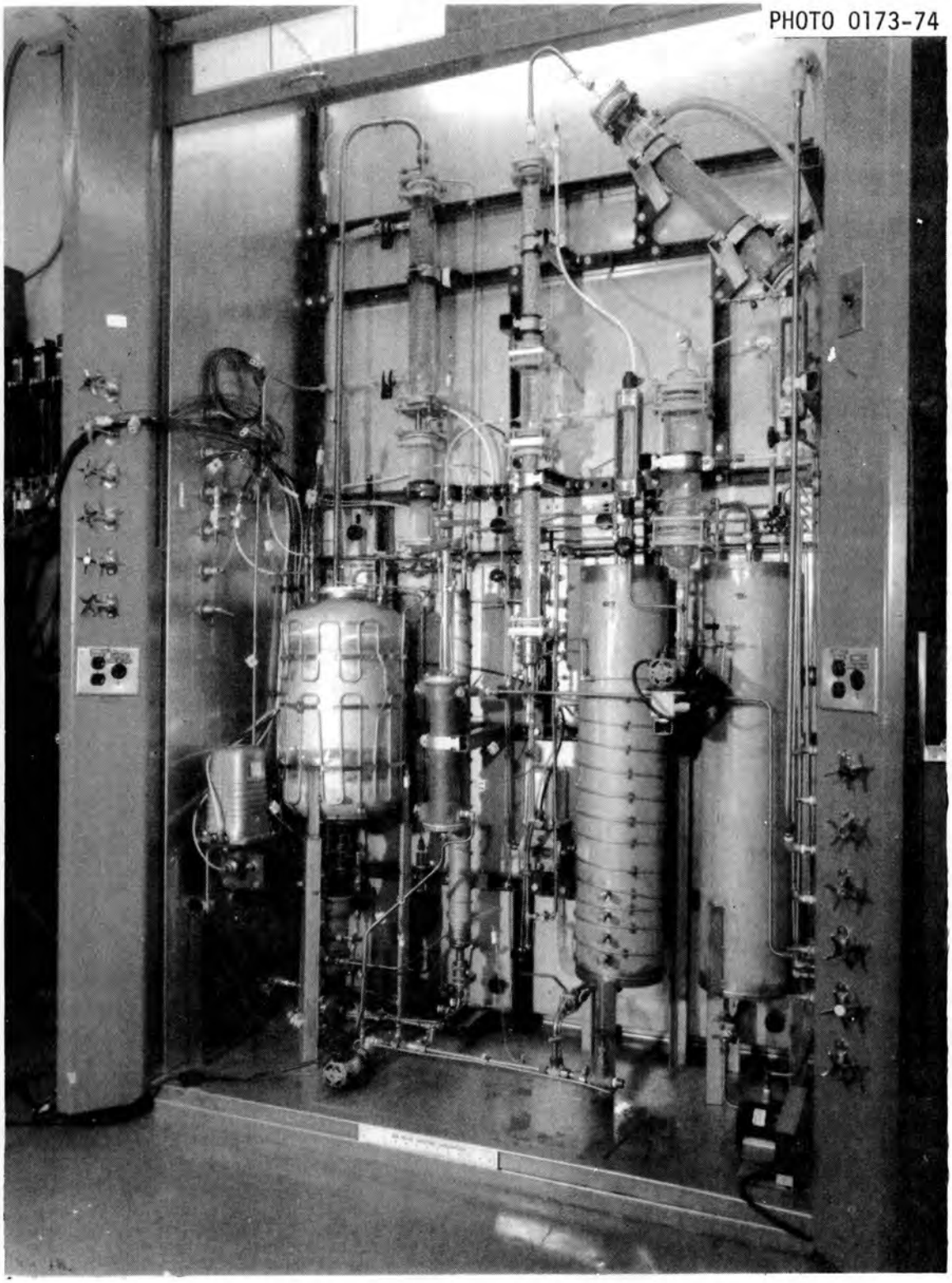

Fig. 10-3. Bench-Scale Equipment for Nitric Acid Production by Extractive Distillation. Equipment ready for application of thermal insulation.

T5 before disposal. Wet-air cooling of heat exchanger HX1 drops the temperature about 10°C for the recirculating solution entering the pump. In a separate operation, the 74 wt % $Mg(NO_3)_2$ solution at about 130°C is metered to column C7 through a throttling valve at a rate which is inferred from the draw-down rate for calibration tank T6. Pump P3 meters dilute room-temperature HNO_3 to the mixing section at the mid-point of the column. The resulting concentrated nitric acid vapors pass through the packed rectifying section into the 3.5-ft^2 QVF condenser. Condensate is collected in tank T4, from which reflux pump P2 returns acid at any desired reflux ratio. From the mixing section of the column the relatively dilute $Mg(NO_3)_2$ solution flows downward through the stripping section, where a metered steam flow strips nitric acid from the solution before it leaves the column and collects in tank T2. Liquid samples can be taken from the column directly below the mixing section, and at the bottom of the stripping section. The semicontinuous process employed here is completed when the dilute $Mg(NO_3)_2$ solution is returned to tank T1 for reconcentration.

Initial shakedown work was confined to the magnesium nitrate portion of the system. A magnetically-coupled centrifugal pump operating at a reduced speed of 4200 rpm produced satisfactory flow rates of about 3000 to 6000 g/min of magnesium nitrate solution to the principal heat exchanger over the concentration range of interest, 58 to 74 wt % $Mg(NO_3)_2$. Condensate rates ranged up to about 35 ml/min for ~ 60 wt % solution, using 100-psi steam pressure. Steam pressure up to 230 psi was required for the final concentration step. Pumping methods which did not work satisfactorily, because of the high viscosity of the solution, were a magnetically-coupled gear pump and a magnetically-coupled centrifugal pump operating at 9000 rpm.

10.3 Density of $Mg(NO_3)_2$ Salts at Elevated Temperatures

(R. H. Rainey)

The densities of magnesium nitrate salts containing three and six waters of hydration have been determined at temperatures above their melting points to about 240°C. The density decreased nearly linearly with temperature. The density of $Mg(NO_3)_2 \cdot 6\ H_2O$ decreased from 1.575 at 100°C to 1.461 at 240°C, whereas that for $Mg(NO_3)_2 \cdot 3\ H_2O$ decreased from 1.728 at 130°C to 1.659 at 240°C. The least squares fit to these data is given by the following equations:

$$d_{(3H_2O)} = 1.8284 - 0.000705\ t^\circ \text{ and}$$

$$d_{(6H_2O)} = 1.6556 - 0.000818\ t^\circ\ .$$

The correlation coefficients for these data are 0.9935 and 0.9929, respectively.

10.4 Equilibrium in the Oxidation of Iodine by Hyperazeotropic Nitric Acid

(J. C. Mailen, W. B. Howerton, and C. T. Thompson)

The oxidation of iodine by hyperazeotropic nitric acid to yield non-volatile forms of iodine is the basis for the Iodox process[1-3] for trapping radioiodine. In this process, air containing radioiodine is contacted in a countercurrent flow column with hyperazeotropic nitric acid. The iodine is oxidized and held in the acid phase for later concentration and disposal.

Studies of the kinetics of the oxidation of iodine by hyperazeotropic nitric acid[4] indicate that the oxidation proceeds in at least two sequential steps, the first of which is oxidation of iodine to the +1 valence.

We have measured equilibria for the oxidation of I^0 to I^+ at 25°C in 14.6 to 19 *M* nitric acid. Two determinations for the equilibrium in the oxidation of I^+ to IO_3^- were also made.

Materials Used. - The nitric acid solutions were prepared by dilution of fuming nitric acid, and were air-sparged to remove oxides of nitrogen prior to use. Reagent grade potassium iodide, potassium iodate, and sodium nitrite were used as the sources of iodine and nitrite. All solutions and dilutions used triply distilled water.

Apparatus. - A Beckman DB-1 spectrophotometer was used to determine I_2 and N_2O_4 concentrations. Sealed cells with a 1-cm path length were used and the cell compartment was air-cooled to maintain the temperature at approximately 25°C. Absorbance was shown to be linear with concentration to absorbances of about 1.2 and 1.8 at 340 and 400 nm, respectively. Absorbance determinations were used for analytical purposes up to absorbances of 1.0. Molar absorptivities of analytical nitrite and iodine in concentrated nitric acid were determined earlier.[4] The molar absorptivity of iodine was found to be about 700 liters $mole^{-1}$ cm^{-1} at 470 nm. The molar absorptivity of analytical nitrite varied from 500 liters $mole^{-1}$ cm^{-1} in 15 *M* nitric acid up to 650 liters $mole^{-1}$ cm^{-1} in 20 *M* acid.

Procedure. - Before beginning the series of experiments, standard KI and nitrite solutions were prepared. The KI solution was made up gravimetrically to be 0.5107 *M* in KI, and was found by analysis to be 0.504 *M*. The gravimetric value was used in all calculations. A standard $NaNO_2$ solution was made up gravimetrically to be 1.277 *M* and was found by analysis to be 1.30 *M*. At the end of the series of experiments it was reanalyzed and found to be 1.28 *M*. All standard solutions were stored in large glass bottles with polyethylene seals. The main solution bottles were opened only infrequently to remove volumes for filling secondary standard bottles. This procedure minimized exposure to air and contributed to the stability of the nitrite standard.

In the earlier kinetic studies we observed that the first reaction of iodine to give what appeared to be the +1 valence was much more rapid than subsequent further oxidation of the iodine. This suggested that study of

the equilibrium in the first reaction might be relatively easy. Values of the first equilibrium constant have been determined using two techniques. First a small quantity of a standard KI solution was added to nitric acid contained in a spectral cell and the cell was then sealed and the contents mixed. After the absorbance of I_2 at 470 nm had ceased to decline, the analytical nitrite absorbance at 350 nm was examined. This absorbance was then blanked out by several small additions (successively smaller as the proper concentration was approached) of standard nitrite solution to the reference cell. The total volume of nitrite standard (1.28 *M* or, in a few cases, 5 *M*) was limited to less than 10 μl to prevent any significant change in the acid concentration in the reference cell. These additions were made using a Pipetman adjustable automatic pipette (0 to 20 μl), which was tested and found to be accurate to ± 2 to 4% and precise to ± 1 to 2% over the 5 to 20 μl range. The analytical nitrite concentration in the sample cell was taken as that which, when added to the reference cell, gave a 100% relative light transmission of the sample in the region of the analytical nitrite peak. The concentration of iodine was then determined by its absorbance at 470 nm. A molar absorptivity of 700 liters $mole^{-1}$ cm^{-1} (the value found previously[4] in 15.5 and 17.5 *M* nitric acid) was used for iodine. The quantity of iodine in the +1 and +5 oxidation states was determined by material balance using the amount of I^0 remaining and the amount of analytical nitrite formed. All the iodine which had disappeared must have gone at least to the +1 state, and any analytical nitrite produced above that formed in this reaction is attributed to +5 iodine formation. These data then allow calculation of the equilibrium constant. It should be noted that, in these tests, the system was not allowed to reach final equilibrium; this requires many hours. Thus, the equilibrium constant for the reaction of +1 iodine to form +5 iodine cannot be calculated from these data. A second method for determining K_1 was to add equal, relatively large quantities of nitrite to the sample and reference cell mixtures already discussed. The further reaction of I^+ to form IO_3^- should produce two moles of analytical nitrite per I^+, making this reaction relatively easy to reverse by adding large quantities of nitrite. After this is done, the I^+ content of the nitric acid can be taken as the initial iodine minus the iodine present as I_2 after the addition.

In two cases solutions were allowed to sit for several days to reach complete equilibrium. The concentration data from these tests was used to calculate values of the equilibrium constant for the oxidation of I^+ to IO_3^-.

Expected Reactants and Products. - The earlier kinetic studies showed that the reaction rate constant for I_2 oxidation increases very rapidly with increasing nitric acid concentration above the azeotrope. This suggests that the reaction involves molecular HNO_3, the activity of which increases quite rapidly above the azeotrope.[5] The compound INO_3 has been reported to exist in nitric acid.[6] We will assume this as the +1 iodine product in this study. It could conceivably exist as the compound INO_3 or as an ionic species. Since the material is very dilute in these tests, we will assume the ionic form. The equilibrium data for nitrogen oxides in contact with concentrated nitric acid[7] lead to the conclusion that NO_2 or N_2O_4 is the likely form for the reduced nitrogen

oxide product. Air-liquid distribution data for NO_2 between air and concentrated nitric acid (see Sect. 10.5) indicate a dimeric form in the acid, so we will assume N_2O_4 as the product. The analytical nitrite concentration calculated from the additions of standard nitrite is equivalent to N_2O_4 by:

$$HNO_2 + HNO_3 \rightarrow N_2O_4 + H_2O \ . \tag{1}$$

The product which precipitates from hyperazeotropic nitric acid[8] saturated with +5 valence iodine is HI_3O_8. Based on this information it is likely that +5 valence iodine exists in solution as the IO_3^- ion. From these considerations the two equilibrium reactions will be written as:

$$I_2 + 4HNO_3 \rightleftarrows 2I^+ + 2NO_3^- + N_2O_4 + 2H_2O \ , \tag{2}$$

$$I^+ + 3HNO_3 + NO_3^- \rightleftarrows IO_3^- + H^+ + 2N_2O_4 + H_2O \ . \tag{3}$$

<u>Experimental Equilibria: Oxidation of I^o to I^+.</u> - At any one nitric acid concentration the equilibrium constant for reaction (2) can be written as:

$$K_{1,E} = \frac{C_{I+}^2 \ C_{N_2O_4}}{C_{I_2}} \ . \tag{4}$$

To facilitate testing the applicability of this equation, logarithms of each side can be taken yielding Eq. (5) after rearranging:

$$\ln \frac{C_{I^+}^2}{C_{I_2}} = - \ln C_{N_2O_4} + \ln K_{1,E} \ . \tag{5}$$

Thus, a log-log plot of $C_{I^+}^2 / C_{I_2}$ vs $C_{N_2O_4}$ should give a straight line of -1 slope for each acid concentration. These plots are shown in Fig. 10-4 with lines of -1 slope drawn through each set of data. The slopes of -1 are seen to fit the data reasonably well demonstrating that these data are consistent with the reaction (2). If the overall reaction of I_2 to give IO_3^- had been measured, the slopes should have been -5.

If the overall reaction to form I^+ is as given in reaction (2), then the true equilibrium constant can be written as:

$$K_1 = \frac{a_{I^+}^2 \ a_{NO_3^-}^2 \ a_{N_2O_4} \ a_{H_2O}^2}{a_{I_2} \ a_{HNO_3}^4} \ . \tag{6}$$

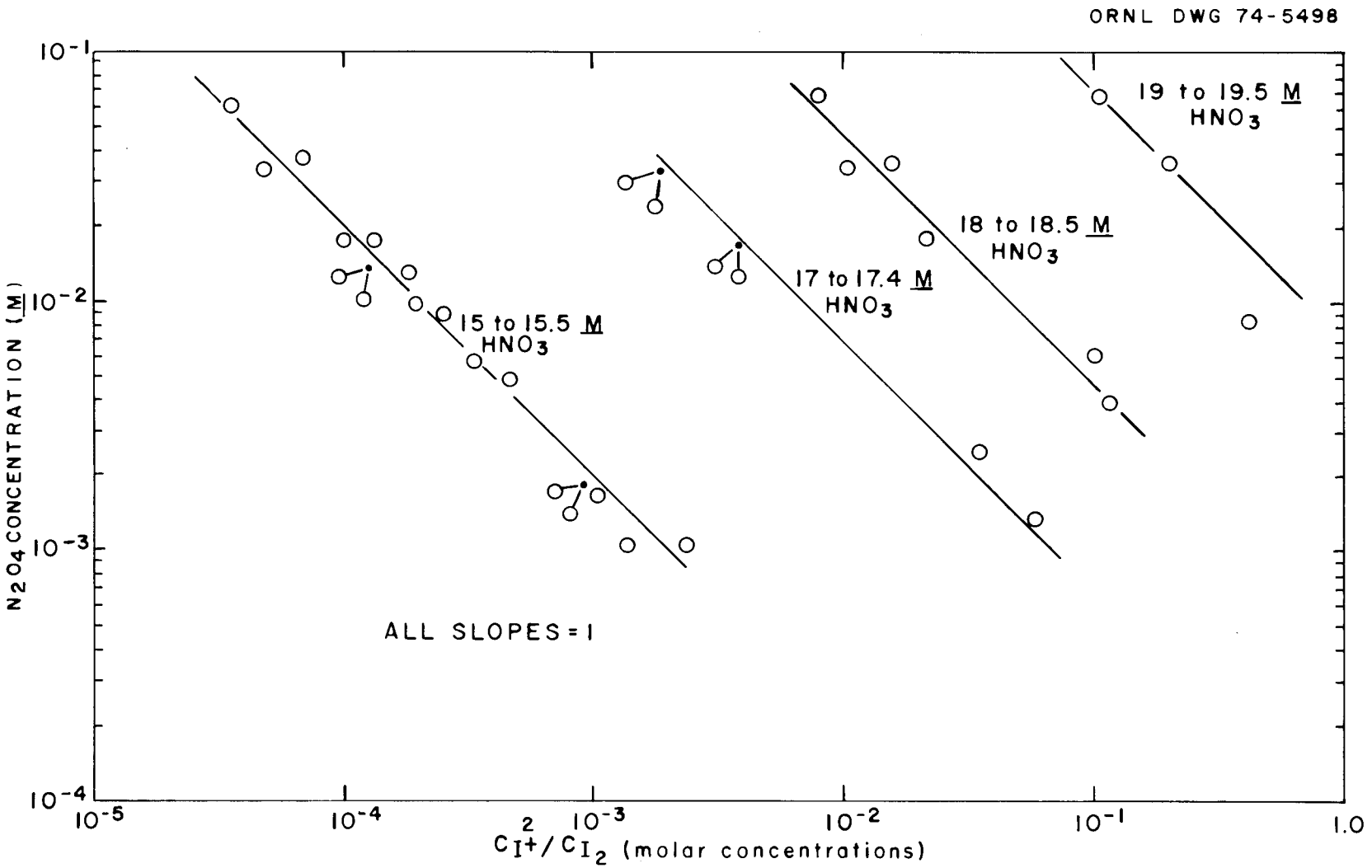

Fig. 10-4. First Power Dependence of $K_{1,E}$ on N_2O_4 Concentration.

Since our solutions were very dilute in iodine species and in N_2O_4, the activities of HNO_3, NO_3^-, and H_2O can be taken as those for the pure acid. Values of these have been compiled and tabulated by Davis and DeBruin.[5] We can now break K_1 up into quantities which are related to the experimental measurements, those for pure nitric acid, and those for which values are unknown as is shown below:

$$K_1 \quad K \; \frac{C_{I^+}^2 \; C_{N_2O_4}}{C_{I_2}} \cdot \frac{a_{H_2O}^2 \; a_{NO_3^-}^2}{a_{HNO_3}^4} \cdot \frac{\gamma_{I^+} \; \gamma_{N_2O_4}}{\gamma_{I_2}} \tag{7}$$

From the experimental data only the total +1 valence iodine can be calculated. This will include both I^+ and any combined forms such as INO_3. To analyze the data further requires that we assume that the combined forms are only a small fraction of the total +1 valence iodine. Some information regarding the activity coefficients in the last term can be obtained from gas-liquid distribution coefficients. The distribution of iodine between air and nitric acid changes very slowly between 10 and 16 *M* nitric acid,[9] indicating that γ_{I_2} is not greatly affected by changes of nitric acid concentration. Distribution data in more concentrated acid has not been obtained due to the rapid reaction of I_2 with hyperazeotropic nitric acid. The distribution of N_2O_4 to air from nitric acid decreases by a factor of 3.3 with the same gas phase concentration between 15.7 and 19 *M* nitric acid, indicating a similar change of the activity coefficient in nitric acid. Nothing is known of the activity coefficient for I^+, but based on the relatively small change in the other activity coefficients we will assume that the last term in Eq. (7) changes very little and can be combined into K_1 as shown below:

$$K_1' = \frac{C_{I^+}^2 \; C_{N_2O_4}}{C_{I_2}} \cdot \frac{a_{H_2O}^2 \; a_{NO_3^-}^2}{a_{HNO_3}^4} , \tag{8}$$

$$K_1' = K_{1,E} \cdot K_{1,A} . \tag{9}$$

Taking logarithms of each side of Eq. (9) and rearranging gives:

$$\ln K_{1,E} = - \ln K_{1,A} + \ln k_1' . \tag{10}$$

Thus, if all the assumptions are reasonable or if the neglected effects cancel out, a log-log plot of $K_{1,E}$ vs $K_{1,A}$ should be linear and have a slope of -1. Figure 10-5 shows this plot with the least-squares linear fit shown as a dashed line and the least-squares-determined line of -1 slope shown as a solid line. The least-squares line without restriction on the slope has a slope of -0.927 ± 0.046 (95% confidence

ORNL DWG. 74-5499

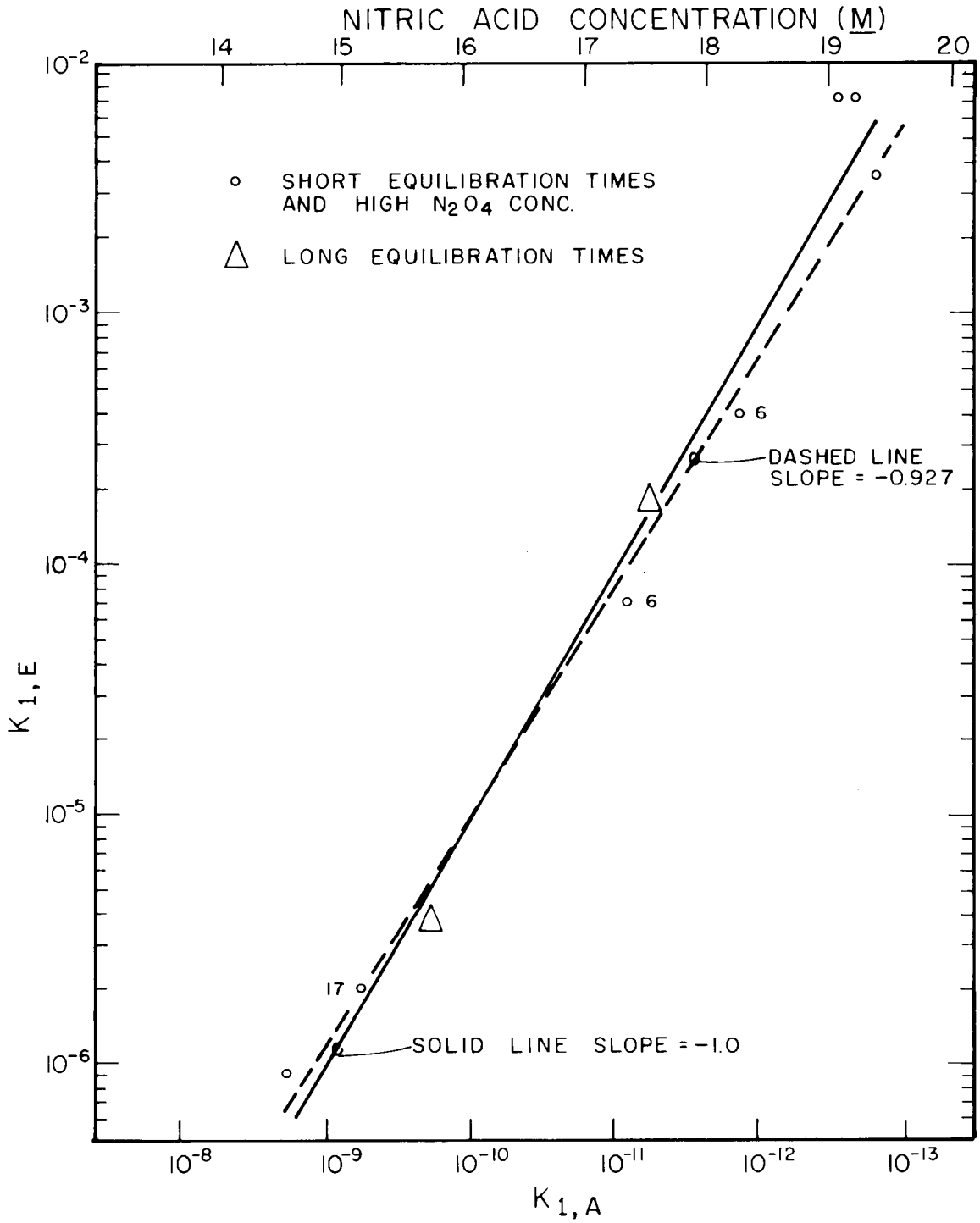

Fig. 10-5. $K_{1,E}$ vs $K_{1,A}$. (Numbers beside points indicate number of determinations averaged to obtain the point.)

limits). The fact that the slope is close to -1 and that the straight line correlation looks reasonable indicates that the data are consistent with the reactants and products given in Eq. (2). Assuming that the -1 slope is correct, the equilibrium constant for reaction (2) can be written:

$$\frac{C_{I^+}\ C_{N_2O_4}\ a^2_{H_2O}\ a^2_{NO_3^-}}{C_{I_2}\ a^4_{HNO_3}} = 9.74 \times 10^{-16} \qquad (11)$$

over the range of 15 to 19 *M* nitric acid at 25°C.

Experimental Equilibria: Oxidation of I^+ to IO_3^-. - In two successful tests the samples were allowed to sit for several days to attain complete equilibrium among all the species. In a test using 15.8 *M* nitric acid, a solution containing 0.01 *M* HIO_3 in 15.8 *M* nitric acid was prepared. This solution was then made 4.25×10^{-3} *M* in NO_2^- and was sealed in a Teflon-capped glass bottle for 22 days. At the end of this time a spectral scan of the solution determined the concentrations of I_2 and N_2O_4 and from these, by material balance, the concentrations of IO_3^- and I^+ were calculated. In a test using 17.6 *M* nitric acid, a portion of standard KI solution was added to 18 *M* nitric acid, the solution was held for four days in a Teflon-capped glass bottle and analysis was the same as for the 15.8 *M* case. Attempts to measure the equilibrium in more concentrated acid were unsuccessful due to three difficulties. First, the equilibrium very much favors complete conversion of all iodine to iodate. This makes it necessary to add so much nitrite to the solution to produce some I_2 that balancing the spectrophotometric cells is difficult. Second, these very concentrated acids slowly decompose with time, making the total reduced nitrogen oxides added and formed difficult to evaluate. Third, the very concentrated acids apparently, over long equilibration times, reacted with small quantities of organics present in the reagents or distilled water to produce additional reduced nitrogen oxides. The values of the experimental equilibrium constants for the two tests are given in Table 10-2, and the two values of $K_{1,E}$ are shown on Fig. 10-5. Note that the calculated concentrations of iodine species assume that iodine exists only in the 0, +1, and +5 valence states. The fact that the values of $K_{1,E}$ agree well with the values determined where the N_2O_4 concentration was high (valences other than 0 and +1 for iodine are minimized) indicates that species such as +3 valence iodine are not important. If this is true, we can use the calculated IO_3^- concentration to evaluate the equilibrium constant for reaction (3).

We can write the equilibrium constant for reaction (3) as:

$$K_2 = \frac{a_{IO_3^-}\ a_{H^+}\ a^2_{N_2O_4}\ a_{H_2O}}{a_{I^+}\ a^3_{HNO_3}\ a_{NO_3^-}} \ . \qquad (12)$$

Table 10-2. Values of Equilibrium Constants for Long-Time Equilibrations

HNO_3 (*M*)	$K_{2,E}$	$K_{2,A}$ (ref. a)	K'_2
15.8	3.43×10^{-6}	8.40×10^{-11}	2.88×10^{-16}
17.6	5.68×10^{-5}	4.86×10^{-12}	2.76×10^{-16}

[a] Values of $K_{2,A}$ calculated from data in Reference 5.

This can be divided into three terms:

$$K_2 = \frac{C_{IO_3^-} C^2_{N_2O_4}}{C_{I^+}} \cdot \frac{a_{H^+} a_{H_2O}}{a_{NO_3^-} a^3_{HNO_3}} \cdot \frac{\gamma_{IO_3^-} \gamma^2_{N_2O_4}}{\gamma_{I^+}} . \qquad (13)$$

Since we are dealing with nearly pure solvent, the concentrations of H^+ and NO_3^- are equal and, since we are using the mean ionic activity coefficient for them, we can cancel out a_{H^+} and $a_{NO_3^-}$ from Eq. (13).

From material balance we can calculate only the total +5 valence iodine, and we will assume that all is present as IO_3^-. From solubility data[8] for HI_3O_8 in hyperazeotropic nitric acid, we can estimate the variation in $\gamma_{IO_3^-}$ as the nitric acid concentration is changed. The solubility decreases by a factor of 4.4 between 15.7 and 19 *M* nitric acid. If the dissociation constant for HI_3O_8 in nitric acid is constant over this range of acid concentration, then $\gamma_{IO_3^-}$ will change by a factor of 1.6.

As pointed out in the discussion of the first equilibrium constant K_1, $\gamma_{N_2O_4}$ decreases by a factor of 3.3 over the same acid concentration change. As before, the behavior of γ_{I^+} is unknown, so we assume that the activity coefficient term of Eq. (13) is sufficiently constant to combine it with K_2, giving:

$$K'_2 = \frac{C_{IO_3^-} C^2_{N_2O_4}}{C_{I^+}} \cdot \frac{a_{H_2O}}{a^3_{HNO_3}} , \qquad (14)$$

$$K_2' = K_{2,E} K_{2,A} . \tag{15}$$

The experimental values of $K_{2,E}$, the literature values of $K_{2,A}$, and the calculated values of K_2' are given in Table 10-2. The values of K_2' are seen to differ by only 4%, suggesting that this equilibrium is well represented by the assumed reaction. The equilibrium expression for reaction (3) at 25°C is given below:

$$\frac{C_{IO_3^-} \; C^2_{N_2O_4} \; a_{H_2O}}{C_{I^+} \; a^3_{HNO_3}} = 2.82 \times 10^{-16} ,$$

with the understanding that C_{H^+} and $C_{NO_3^-}$ are equal where all concentrations are molar.

Conclusions. - The study of equilibria in the iodine—nitric acid system confirms the conclusion, from kinetic studies, that the oxidation of iodine occurs in at least two sequential steps. The equilibrium data is consistent with the existence of only two steps, the first involving the oxidation of I_2 to I^+ and the second being the oxidation of I^+ to IO_3^-. However, the existence of other components at relatively low concentrations cannot be eliminated.

10.5 Equilibrium of NO_2 Between Nitric Acid and Air

(J. C. Mailen and W. B. Howerton)

When iodine or organic iodide compounds react with nitric acid, nitrogen oxides are produced by reduction of nitric acid. In hyperazeotropic nitric acid, these should appear as NO_2 or N_2O_4. In the Iodox bubble-cap column the NO_2 will distribute between the nitric acid and air streams; knowledge of this distribution is necessary for prediction of chemical equilibria within the operating Iodox column.

In these tests, measured volumes of air were sparged through a mixed volume of nitric acid containing nitrogen oxides. The oxides were added as a known volume of standard nitrite solution, and the concentration in the liquid was monitored by measuring the light absorbance at 350 nm. Gas-phase concentration was determined from the difference in the nitrite concentrations of sequential liquid samples. The equilibrium data suggest dimer formation in the liquid phase in accordance with the equilibrium reaction

$$2NO_2(g) \rightleftarrows N_2O_4(\ell) .$$

The equilibrium constant K for this reaction is given by:

$$K = \frac{[N_2O_4(\ell)]}{[NO_2(g)]^2} ,$$

in which the brackets denote molar concentration. The experimental values of K can be described analytically by the empirical expression

$$\ln K = 24.651 - 2.015\ (HNO_3) + 0.06685\ (HNO_3)^2 ,$$

which is applicable over the HNO_3 concentration range 15.7 to 20 *M*.

10.6 Selective Absorption of Krypton and Xenon

(M. J. Stephenson and W. D. Reed)

The primary absorption-stripping section of the selective absorption pilot plant is ready for operation. Shakedown operations for this part of the facility were completed last quarter. Installation of the process subsystems is continuing close to schedule. At present, the solvent purification still is ready for service and the product purification and solvent recovery sorbent traps have been installed; however, process piping and instrumentation are not yet completed. No further progress can be made on the feed gas preparation station until mass flowmeters and controllers are received from the manufacturer. The total pilot facility is expected to be ready for operation at the first of the coming fiscal year.

References for Sect. 10

1. Chem. Technol. Div. Ann. Progr. Rept. March 31, 1972, ORNL-4794 (August 1972), p. 21.

2. Chem. Technol. Div. Ann. Progr. Rept. March 31, 1971, ORNL-4682 (July 1971), pp. 61-62.

3. LMFBR Fuel Cycle Studies Progr. Rept. for March 1972, No. 37, ORNL-TM-3807 (April 1972), pp. 11-18.

4. J. C. Mailen and T. O. Tiffany, submitted to J. Inorg. Nucl. Chem.

5. W. Davis, Jr., and H. J. DeBruin, J. Inorg. Nucl. Chem. 26, pp. 1069-1083.

6. M. Schmeisser and K. Brandle, Angew. Chem. 73, 388-393 (1961).

7. L. Ya. Tereschenko et al., Zh. Prikl. Khim. 41, 702-9 (1968).

8. R. H. Rainey and J. C. Mailen, J. Chem. and Engr. Data (in press).

9. LMFBR Fuel Cycle Studies Progr. Rept. for May 1972, No. 39, ORNL-TM-3888 (July 1972), p. 20.

11. ENGINEERING STUDIES (TASK 11)

(A. R. Irvine and E. L. Nicholson)

The purpose of this task is to examine the overall problem of LMFBR spent fuel recovery plant design and to relate the individual problems involved in fuel recovery to the overall problem and to the other individual problems. Individual problems to be evaluated range from special problems in safety and containment (which are peculiar to reprocessing of LMFBR spent fuel) to equipment design and operational procedures.

Observations Concerning Volatile Fission Product Confinement System

The process options for confinement of the volatile fission products in a commercial-scale reprocessing facility have been examined. The volatile fission products of concern are iodine, krypton, and xenon.

While the criterion for iodine retention will be governed primarily by the preprocessing decay period (at decay times $\leq$ 180 days), the criteria for macro and micro removal of iodine from off-gas are somewhat flexible. At very short decay times (30 to 50 days), the total average iodine confinement factor must be $\geq 10^9$. This confinement factor could conceivably be obtained by getting a DF of 10^7 by either of the two processes, with the other process being required to obtain a DF of 10^2. From a practical standpoint, it is prudent to provide a wide margin of DF capability under "normal" operating conditions to allow for periods of misoperation. The micro-iodine removal system is to serve not only as the final iodine removal device but also as a reserve system for total iodine removal in the event of failure (for whatever reason) of the macro-iodine removal system. Imposition of "reserve unit status" on the micro-iodine removal system leads to the conclusion that it should be (a) provided with ample reserve iodine-holding capacity, (b) provided with deep beds to yield very high iodine DFs, (c) protected against poisoning by spurious chemicals, (d) monitored continuously for adequacy of operation, and (e) provided in duplicate with a spare unit held in reserve. Tests by R. D. Ackley et al. have indicated that silver zeolite is the most desirable material available for use in micro-removal of iodine from off-gas.

The above militate for the use of the most effective macro-iodine removal system available, which is Iodox. The design objective for DF obtained by this system should be at least 10^6, for the simple reason that it apparently can be obtained with a gas-liquid contactor of reasonable length. The gas from the Iodox contactor must be scrubbed to remove acid vapors and nitrogen oxides. The water used for scrubbing must be essentially free of iodine or it will add to the iodine content of the off-gas. The iodine content of this water can be reduced to a low level by evaporative and sorption processes. The ^{131}I content of water used for this purpose can be reduced to truly negligible levels by decay-storage.

The subsequent process for noble gas retention requires the feed gas to be compressed to about 20 atm and to have a low dew point. Hence, the

nitrogen oxide scrubbing step may be accomplished at elevated pressure, where its effectiveness is much greater. If the gas is then dried, the effectiveness of all of the micro-iodine removal processes, including silver zeolite, is increased. Under this concept, the silver zeolite sorbers would be operating at elevated pressure and near ambient temperature instead of ambient pressure and high temperature with a high absolute water content. No data are available at elevated pressure, although other data do indicate excellent performance of silver zeolite at ambient temperature and low relative humidity.

Examination of the available information on noble gas recovery has indicated a need for resolution of certain questions before a preferred option for this process step can be selected. These questions are:

1. Does a method exist which will essentially eliminate explosion hazards in a cryogenic distillation system for noble gas recovery from a fuel reprocessing plant?

2. How would total installed costs and total operating costs for cryogenic and selective absorption systems appropriate for an LMFBR fuel reprocessing plant compare?

A paper presented at the Noble Gases Symposium at Las Vegas in September 1973 by J. S. Davis and J. R. Martin, entitled, "A Cryogenic Approach to Fuel Reprocessing Radwaste Treatment," indicates a positive answer to the first question. A variety of estimates of noble gas recovery equipment costs presents a confused picture with respect to the second question.

ORNL-TM-4587
UC-79c - Fuel Recycle

INTERNAL DISTRIBUTION

1. R. D. Ackley
2. R. E. Blanco
3. J. O. Blomeke
4. W. D. Bond
5. R. E. Brooksbank
6. K. B. Brown
7. F. R. Bruce
8. D. A. Canonico
9. G. I. Cathers
10. J. M. Chandler
11. S. D. Clinton
12. C. F. Coleman
13. L. T. Corbin
14. D. A. Costanzo
15. D. J. Crouse
16. F. L. Culler
17. W. Davis, Jr.
18. D. E. Ferguson
19. L. M. Ferris
20. C. L. Fitzgerald
21. J. D. Flynn
22. M. H. Fontana
23. H. W. Godbee
24. J. H. Goode
25. A. T. Gresky
26. W. S. Groenier
27. P. A. Haas
28. B. A. Hannaford
29. W. O. Harms
30. F. E. Harrington
31. R. B. Heimdahl
32. D. E. Horner
33. A. R. Irvine
34. P. R. Kasten
35. L. J. King
36. B. B. Klima
37. R. E. Leuze
38. B. Lieberman
39. A. L. Lotts
40. R. S. Lowrie
41. R. E. MacPherson, Jr.
42. J. C. Mailen
43. A. P. Malinauskas
44. W. T. McDuffee
45. L. E. McNeese
46. J. P. Nichols
47. E. L. Nicholson
48. J. R. Parrott
49. A. M. Perry
50. H. Postma
51. R. H. Rainey
52. A. D. Ryon
53. W. F. Schaffer, Jr.
54. C. D. Scott
55. L. B. Shappert
56. W. E. Shockley
57. J. W. Snider
58. M. J. Stephenson
59. D. B. Trauger
60-62. W. E. Unger
63. V. C. A. Vaughen
64. C. D. Watson
65. G. A. West
66. R. G. Wymer
67. O. O. Yarbro
68. H. C. Young
69. Laboratory Records, RC
70-71. Central Research Library
72. Document Reference Section
73-82. Laboratory Records
83. ORNL Patent Office
84. Nuclear Safety Information Center

EXTERNAL DISTRIBUTION

85. Research and Technical Support Division, AEC-ORO
86. RRD Senior Site Representative, D. F. Cope, at ORNL
87-88. Director, Division of Reactor Research and Development, U. S. Atomic Energy Commission, Washington, D. C. 20545
89-317. Given distribution as shown in TID-4500 under UC-79c, Fuel Recycle Category